TRI-PP-93-71
Aug 1993

The Elastic and Inelastic Scattering of Intermediate Energy Protons on Deuterium at Small Momentum Transfer

S. Burzynski[1†], K.P. Jackson[2], W.P. Alford[3], J.E. Cromer[2], R. Helmer[2], B.E. King[2], I. Šlaus[4], B. Spicer[5], A. Trudel[1] and S. Yen[2]

[1] Simon Fraser University, Burnaby B.C., Canada V5A 1S6
[2] TRIUMF, 4004 Wesbrook Mall, Vancouver B.C., Canada V6T 2A3
[3] Physics Department, University of Western Ontario, London, Ontario, Canada N6A 3K7
[4] Rudjer Boškovic Institute, 41000 Zagreb, Croatia
[5] School of Physics, University of Melbourne, Parkville, Victoria 3052, Australia
[†] On leave from the Soltan Institute for Nuclear Studies, Świerk, Poland

Abstract

The differential cross sections for the elastic and inelastic scattering of protons on deuterium have been measured for scattering angles less than 14° at 198.5, 297.6 and 456.6 MeV. These quantities were determined relative to $d\sigma/d\Omega$ for pp elastic scattering with a precision of typically 2%. The range of excitation energies for the (p,p') reaction was chosen to emphasize the region near the np threshold dominated by the final-state interaction in the $^1S_0$ channel. Particular attention was given to the dependence on excitation energy of the spectra at 198.5 MeV to examine the sensitivity to the $^1S_0$ scattering length, a_{np}. In this paper all data are compared with a new, general formulation of a simple model of the reaction mechanism based on the impulse approximation. The experimental results differ from the predictions by typically 10% and the differential cross sections exhibit a sensitivity to the intermediate-energy nucleon-nucleon amplitudes. If the impulse approximation is used to estimate a_{np} from the data at 198.5 MeV a value of -24.7 ± 0.4 fm is obtained.

E NUCLEAR REACTIONS: ^{2}H(p,p_0), ^{2}H(p,p'), E=198.5, 297.6, 456.6 MeV; measured $\sigma(E;E_p,\theta)$. Enriched target.

(submitted to Nuclear Physics A)

1. Introduction

The scattering amplitudes which define the nucleon-nucleon (NN) interaction at intermediate energies are sensitive to both spin and isospin. This sensitivity is exploited in studies of nucleon-nucleus (NA) scattering to achieve a better understanding of the simple modes of nuclear excitation particularly those involving a change in spin or isospin of a single nucleon in the target. This goal is most readily achieved when the NA measurements can be most directly related to the known properties of the NN interaction.

This paper describes the results of precise measurements of the differential cross-sections for the scattering of protons of three energies (E_i = 198.5, 297.6 and 456.6 MeV) at small angles ($3° \leq \Theta \leq 14°$) from the lightest nuclear target, deuterium. The spectra of the scattered protons are recorded as a function of the energy loss ($\omega = E_i - E_f$) over an energy range that includes elastic scattering (p,p_0) and inelastic scattering (p,p') to unbound states in the final np continuum at excitation energies (ε) up to 5 MeV above the energy of the deuteron ground state ($\varepsilon = 0$). These conditions should ensure the simplest possible interpretation of the data in terms of the NN amplitudes at these incident energies, and the well-studied properties of both the deuteron and the np scattering states at low values of ε.

The deuteron is known to have quantum numbers J^π, $T = 1^+$, 0 and the largest component of the wave function is $^{2S+1}L_J = {}^3S_1$. In addition, the np scattering states just above the threshold at $\varepsilon = 2.2245$ MeV are strongly influenced by the final-state interaction in the $^1S_0$, $T = 1$ channel. The consequence of these simple configurations is that the limited range in ε includes both the elastic scattering and the simplest nuclear Gamow-Teller transition ($\Delta L = 0, \Delta S = \Delta T = 1$). The deuteron offers a unique opportunity to relate precise data on both these processes to the NN amplitudes. It should be noted that the Gamow-Teller transition investigated in the (p,p') reaction is the analogue of that involved in the fundamental reaction in nuclear astrophysics, $p + p \rightarrow d + e^+ + \bar{\nu}$ [ref.[1])].

In the spirit of testing a simple model of the nuclear reactions observed, the experimental results are compared with a new, detailed formulation of the impulse approximation (IA) defined explicitly in sect. 4. This approximation[2]) relates directly the elastic[3]) and inelastic[4]) scattering of protons from deuterium to the NN amplitudes at the same values of E_i and Θ measured in the laboratory frame. It is well known that the IA is not a complete theory of NA scattering but unless data exist which quantitatively define the failure of the simplest model it is difficult to assess the significance of the success of the refinements which address the physics "beyond" the simplest model. The conditions chosen for this experiment are almost ideally suited to the application of the IA.

Measurements at 158 MeV of the elastic and inelastic pd scattering for the purpose of comparison with the predictions of the IA were published 30 years ago by Stairs *et al.*[5]). Their results for the differential cross sections for the $d(p,p_0)$ reaction at $\Theta < 15°$ were generally consistent (within ±10%) with the predictions of the IA based on the then existing partial wave analysis of the NN data. Their measurements of $d^2\sigma/d\Omega dE$ for the $d(p,p')$ reaction, however, exceeded the corresponding predictions of the IA by between 15 and 50%. The (p,p') results were, however, challenged by those of Kuroda *et al.*[6]) for the $d(p,p')$ reaction at 150 MeV which agreed with

the predictions of Cromer[4]) within the experimental uncertainty of between 5 and 10%. These existing data suggest that the predictions of the IA are possibly valid at the level of ±10% under the condition investigated in the present experiment.

To be sensitive to any of the processes not included in the IA (such as multiple scattering or off-shell effects) measurements with a precision of at least ±2% are clearly required. To achieve this precision the present experiment utilizes a magnetic spectrometer with a broad, carefully-calibrated momentum acceptance and a unique technique involving a mixed target of liquid hydrogen and deuterium. Also of crucial importance is the dispersion matching in momentum of the incident proton beam and the spectrometer to achieve a resolution in energy loss (ω) of typically 90 keV. This resolution combined with exceptional care in the energy calibration of the spectra are also essential elements in achieving the additional goal in this experiment which is a precise measurement of the shape of the $d(p,p')$ spectra near the np threshold and the interpretation of these results in terms of a_{np} the np $^1S_0$ scattering length.

The neutron-neutron scattering length a_{nn} and the corresponding value of the effective range r_e are defined by the behavior of the $^1S_0$ phase shift δ_0 at the lowest values of k, the relative momentum of two nucleons:

$$k \cot \delta_0 = -1/a + \frac{1}{2} r_e k^2 + ... \qquad (1)$$

A comparison of a_{nn} and a_{pp}^N (the corresponding value for the pp interaction after corrections for the influence of the electromagnetic interaction) is an important measure of the charge symmetry breaking in the strong interaction[7]). A direct measurement of a_{nn} has not been performed. Consequently, much experimental and theoretical effort has been devoted to the determination of this quantity from reactions involving more than two particles. The presently recommended value of $a_{nn} = -18.52 \pm 0.34$ fm[8]) is based mainly on a single $d(\pi^-,\gamma)2n$ experiment[9]) supported by the results using the same reaction in a kinematically complete configuration[10]). An independent confirmation of this result by a completely different technique would be very desirable.

Many attempts have been made to estimate a_{nn} on the basis of detailed studies of the $d(n,p)2n$ reaction at neutron energies between 14 and 50 MeV. The results, even when analysed using exact three body calculations, produce very scattered results for a_{nn} ranging from -15 to -24 fm[8]). It has been suggested that these results might be reconciled with those of the $d(\pi^-,\gamma)2n$ experiments if one includes effects of the three nucleon force. However, our knowledge of the three nucleon force is far from adequate.

It is argued[8]) that at energies above 60 MeV the effects of the three nucleon force are small. It is certainly true that at intermediate energies the $d(n,p)$ reaction in the forward directions and for small values of k populates the $^1S_0$ states of the nn system by a simpler and more selective reaction mechanism than is in effect at lower neutron energies. The contributions from multiple scattering are reduced and the relative strength of the isovector, spin-flip part of the NN scattering amplitude is larger. These effects are illustrated by the prominent peak attributed to the final state interaction in the $^1S_0$ channel for the data on the $d(p,n)2p$ reaction at 160 MeV[11]) and the succesful interpretation of these data in terms of the IA. The possibility of using the $d(n,p)2n$ reaction at intermediate energies to provide an independent

estimate a_{nn} is enhanced by the prospect of rigorous three body calculations using realistic NN forces at energies up to pion production threshold[12,13]).

Before undertaking the technical challenges that must be addressed to obtain a precise estimate of a_{nn} using the $d(n,p)$ reaction at intermediate energies it would be very desirable to have confirmation that the reaction mechanism is adequately understood. In the present experiment very precise data are obtained for the $d(p,p')$ reaction at E_i = 198.5 MeV which then can be used to obtain an estimate of a_{np} for comparison with the value -23.748 ± 0.009 fm[14]) known from low energy np scattering. In this paper the analysis is presented in terms of the simple IA but future refinements of these calculations are expected. The current experimental value $a_{pp}^N - a_{nn} = 1.5 \pm 0.5$ fm is in excellent accord with theoretical predictions based on estimates of the mass difference of the d and u quarks[15,16,7]). To be of significance in this context requires an analysis of the $d(p,p')$ data which determines a value of a_{np} within 0.3 fm of its known value.

The remainder of this paper is organized in the following fashion. A detailed description of the experiment appears in sect. 2 including the results of the several tests and calibrations designed to establish the precision of the final data on the elastic and inelastic pd scattering. In this connection some of the specific details regarding the cryogenic target, the energy calibration and response of the spectrometer and its acceptance are described in appendices A, B, C, and D. The complete experimental results on the $d(p,p_0)$ reaction together with a sample of the $d(p,p')$ data are presented in sect. 3 The explicit formalism used in the analysis of the data in the IA appears in sect. 4 with some of the technical details being presented separately in appendix E. Sect. 5 contains the comparison of the data from this experiment with the predictions of the IA. These comparisons provide a convenient form for a more complete presentation of the $d(p,p')$ data than appears in sect. 3. A discussion of the results of this experiment and a comparison with other related data is in sect. 6 followed by the conclusions presented in sect. 7.

Throughout this paper the energy of the incident proton (E_i), the energy (E_f) and angle (Θ) of the scattered proton as well as all differential cross sections are expressed in the laboratory reference frame. For the unbound states populated in the $d(p,p')$ reaction, ε is the excitation energy measured in the centre of mass of the unobserved np system relative to the deuteron bound state. The following abbreviated notation is used:

$$\sigma_{pp}(\Theta) \equiv \frac{d\sigma}{d\Omega}(\Theta) \qquad (2)$$

for the $p(p,p_0)$ reaction,

$$\sigma_{pd}(\Theta) \equiv \frac{d\sigma}{d\Omega}(\Theta) \qquad (3)$$

for the $d(p,p_0)$ reaction,

$$\sigma_{pd'}(\Theta,\varepsilon) \equiv \frac{d^2\sigma}{d\Omega d\varepsilon}(\Theta,\varepsilon) \qquad (4)$$

for the $d(p,p')$ reaction and

$$\sigma_{pd'}(\Theta) \equiv \int_0^\infty \frac{d^2\sigma}{d\Omega d\varepsilon}(\Theta,\varepsilon) d\varepsilon \qquad (5)$$

for the $d(p,p')$ reaction populating $J^\pi, T = 0^+, 1$ final states. The latter is a quantity derived from $\sigma_{pd'}$ on the basis of the IA as discussed in sect. 5. The quantities are expressed in units with $\hbar$ and $c = 1$.

2. Experimental Details

In the present experiment the differential cross sections σ_{pd} and $\sigma_{pd'}$ were measured relative to σ_{pp} at the same values of E_i and Θ. The ratio σ_{pd}/σ_{pp} was measured using a cryogenic target containing liquid with very nearly equal concentrations of hydrogen and deuterium. The ratio $\sigma_{pd'}/\sigma_{pd}$ was measured as a function of ε using the same target filled with pure liquid deuterium (LD_2). The experimental advantage of measuring these ratios instead of absolute cross sections is that the results are free from uncertainties in the determination of integrated beam intensity, target thickness, the electronic dead time correction, the spectrometer solid angle and the efficiencies of some of the wire chambers involved in the detection of the scattered protons. The measurements were done with protons incident at 198.5, 297.6 and 456.6 MeV using the Medium Resolution Spectrometer (MRS) in the angular range from 3° to 14°. The energies span the range available from the TRIUMF cyclotron and the angles are those conveniently accessible in the small-angle configuration of the spectrometer. The most precise measurements of the dependence of $\sigma_{pd'}$ on ε were made at 198.5 MeV to facilitate future comparisons of the data with rigorous three body calculations.

2.1. EXPERIMENTAL CONFIGURATION AND DATA ACQUISITION

The proton beam was extracted from the TRIUMF cyclotron into beam line 4B (BL4B), dispersed vertically in momentum by 11 cm/% ($\Delta p/p$) and delivered to the target mounted in the T2 scattering chamber on BL4B. The essential features of the configuration of the target and the MRS are shown in fig. 1.

The targets were mounted on the vertically-movable ladder. The cryogenic target containing the liquid deuterium or the liquid deuterium-hydrogen solution was mounted at the top of the ladder immediately below a cooling head. The construction of this target and the procedure to mix the LD_2 and the LH_2 are described in subsect. 2.2. The other targets mounted on the ladder were a ZnS scintillator, an aluminum foil and a graphite sheet. The targets rotated with the spectrometer always having the target plane perpendicular to the axis of the spectrometer.

The trajectory of the scattered protons was sampled at a distance of 107 cm from the target by a front-end chamber (FEC0) comprised of four multi-wire drift chambers. The drift chamber is filled with isobutane at low pressure 30 kPa (0.3 Atm) to minimize multiple scattering, and the spacing of the 16 anode wires in each plane is 5 mm. Two staggered planes of horizontal wires determine the coordinate X0 with a precision of ~ 0.5 mm and Y0 is determined in a similar fashion by the other two wire planes. In order to ensure that the acceptance of the MRS was very nearly constant over the range of momenta sampled in the experiment, FEC0 was used to restrict the analysed data to a rectangle defined by $\Delta X0 = 1.5$ cm and $\Delta Y0 = 4.5$ cm. In order to reduce the effect of high count rates in FEC0 the active area of each plane was masked to an area slightly larger then these software limits.

The magnetic elements of the MRS are a quadrupole followed by a dipole which bends the particles vertically through an average deflection of 60°. The uniform

magnetic field in the dipole B is measured using an NMR probe. For particles centred in the momentum acceptance of the spectrometer the strength of the field in the quadrupole was adjusted to produce a focus in the bend plane at a point just beyond the exit window of the vacuum vessel of the spectrometer. The full momentum acceptance of the MRS is $\Delta p/p \sim 0.15$ and the corresponding focal plane is inclined at an angle of 45° to the central trajectory.

The coordinates of particles passing through the focal plane are determined by four vertical drift chambers mounted in pairs parallel to the focal plane and labelled VDC1 and VDC2 in fig. 1. The chambers X1 and X2 define coordinates in the bend plane and are used by extrapolation to the focal plane to define the momentum of the particle. Because of the length of the focal plane, the transverse coordinates (Y) are derived using the chambers U1 and U2 which have wires inclined at 30° to those in X1 and X2. The design of the VDCs together with their inclination at $\sim 45°$ to the particle trajectories ensures that the ionization from each track is normally sampled by 4 or 5 anode wires which are spaced 0.6 cm apart. The drift times to each wire are measured with TDCs and used to interpolate to the point at which the track passed through the wire plane.

The final element in the MRS detection system used in this experiment was the hodoscope of plastic scintillators located above VDC2. The individual elements were oriented perpendicular to the central trajectory and were spaced to ensure that all particles passed through at least one. The time of passage of a particle through the hodoscope provided a reference for all the timing measurements in this experiment. The energy deposited by a passing particle in any element of the hodoscope (EHOD) was also measured using one ADC channel for each element.

All the relevant data from the wire chambers and scintillators were recorded in event-by-event mode on VCR magnetic tapes on the basis of a hardware trigger. This requirement included pulses in coincidence detected in either X0 or Y0, X1 and a signal in the hodoscope exceeding a preset threshold, as well as a correct time-of-flight between FEC0 and the hodoscope. Although the incident beam intensity was generally < 1 nA the large cross sections for the elastic scattering resulted in valid trigger rates of typically 400 s^{-1}. The data for each event included a TDC channel for each wire hit in all four FEC planes and in all four VDC planes. As a consequence the dead time of the data acquisition computer was substantial. As was mentioned previously, the requirement to measure this dead time accurately was essentially avoided by the measurements of the two ratios σ_{pd}/σ_{pp} and $\sigma_{pd'}/\sigma_{pd}$.

The data written to magnetic tape were subject to several software cuts prior to the creation of the final spectra. The time-of-flight of the particles from FEC0 to the hodoscope was examined to distinguish protons from deuterons or other charged particles emitted from the target. Confirmation of this identification was provided by the signal EHOD. In addition to the minimum requirement of the hardware trigger the hit patterns in all the wire planes in FEC0, VDC1 and VDC2 were analysed to ensure that they were consistent with one and only one charged particle passing through the active region of all the chambers. Events not meeting these requirements were rejected as "missings" or "multiples". The restriction to accept data over the limited region in FEC0 was mentioned previously. In addition a traceback of the trajectories from the VDCs to FEC0 permitted a calculation of the coordinates X1, Y1 at the target. The normal beam profile was ~ 0.3 cm wide $\times$ 2.0 cm high. Any

events originating from outside this region, which might for instance have resulted from beam halo striking the frame of the cryogenic target, were rejected.

2.2. CRYOGENIC TARGET

The planar cell of the cryogenic target was formed by two 50 μm thick foils of hardened aluminum glued and bolted to a rectangular copper frame with rounded corners. The volume of the cell containing the liquid was 7.0 cm high, 3.0 cm wide with a thickness that ranged from 0.6 cm at the edges to 0.8 cm in the central region due to the bulging of the foils. The pressure in the cell during the experiment was typically 50 kPa. Two additional aluminum foils, each 17μm thick were mounted 4.0 cm upstream and downstream of the target as part of an 80° K heat shield. As is mentioned at the beginning of this section the elastic scattering ratios σ_{pd}/σ_{pp} were measured with the cryogenic target filled with very nearly equal concentrations of hydrogen and deuterium. The filling procedure used to achieve this condition, the estimate of the actual ratio and its uncertainty are discussed in detail in appendix A. It is concluded that in all the measurements with the LH_2/LD_2 mixture the ratio of the deuterium to hydrogen nuclei in the target was 1.004 ± 0.010

The investigations of the $d(p,p')$ reaction by measurements of the ratio $\sigma_{pd'}/\sigma_{pp}$ were carried out with the target filled with the pure LD_2. For the most critical measurements with the MRS centred at $\Theta = 4°$ and 8.5°, the deuterium gas used to fill the target was of a purity of 99.99%. However, due to some initial difficulties in filling the target, the LD_2 data at 6° and 11° was recorded with only 99% pure deuterium. The influence on the data analysis of contamination from the $H(p,p_0)$ reaction is discussed in subsect. 5.3.

For the purpose of helping to determine the energy response of the MRS in this experimental configuration spectra were also recorded with the target cell filled with LH_2. The background originating primarily from the aluminum windows and the heat shield, was estimated on the basis of runs taken both with target cell empty and with the pure aluminum foil as a target.

2.3. ENERGY RESPONSE AND CALIBRATION

The magnetic elements of the primary proton beam line were tuned to provide momentum dispersion at the target that matched the vertical dispersion of the spectrometer. Consequently the spectra at the focal plane accurately represented the energy difference, $\omega = E_i - E_f$, despite the energy spread in the incident beam of typically 1 MeV. In addition to providing the focal plane coordinate XF, the measurements of (X0,Y0), (X1,Y1) and (X2,Y2) were used to empirically correct for optical aberrations and kinematic broadening resulting from the finite acceptance of the spectrometer. These corrections were made using the strong elastic scattering peaks observed with the thin carbon and aluminum targets. The resulting resolution in ω was ~ 90 keV, nearly independent of the beam energy.

An important feature of this experiment was the precision required in the energy calibration of the spectra. The most stringent requirement came in the analysis of the data on the $d(p,p')$ reaction in terms of the scattering length a_{np} (see subsect. 5.3). The most critical parameter was the displacement in XF between the location of the $d(p,p_0)$ peak and the $d(p,p')$ threshold corresponding to an excitation energy $\varepsilon = 2224.5$ keV. The precise calibration was also used together with the calculated

kinematic shifts with scattering angle to provide the most accurate estimates of both the average scattering angle for each spectrum and the average incident proton energy E_i.

The relative calibration of the focal plane of the spectrometer was obtained using the calculated differences in momentum for four peaks observed in the scattering of protons from carbon. On the basis of the analysis presented in appendix B, it is concluded that in the spectra with the LD_2 target at 198.5 MeV the location of the threshold at $\varepsilon = 2224.5$ keV was determined relative to $\varepsilon = 0$ with a precision of ± 1.0 keV.

The observed peaks resulting from the scattering of protons on the aluminum, deuterium and hydrogen in the cryogenic target were both substantially broader and more asymmetric than those observed with the thin aluminum and the carbon target. At forward angles with $E_i = 198.5$ MeV the average energy loss of protons passing through the LD_2 target was 600 keV and the observed width (FWHM) of the $d(p,p_0)$ peak was ~ 230 keV. At several stages in the analysis it was essential to have detailed parameterizations of the peak shapes. They could not be adequately predicted on the basis of the thin target spectra by including simple estimates of the effects of the energy straggling and multiple scattering. By analysing the data at several angles with the cryogenic target filled with LD_2, LH_2 as well as the LH_2/LD_2 mixture an empirical representation of the elastic scattering response function was obtained. The details of this procedure are outlined in appendix C.

2.4. SPECTROMETER ACCEPTANCE

Accurate measurements of the ratios σ_{pd}/σ_{pp} and $\sigma_{pd'}/\sigma_{pd}$ as well as the shapes of the $d(p,p')$ spectra required precise information regarding the possible variation of the MRS acceptance as a function of the focal plane coordinate XF. Given this requirement, the data analysed at each setting of the MRS was limited to the range Δ X0 =1.5 cm, Δ Y0 =4.5 cm corresponding to a solid angle $\Delta\Omega = 0.59$ msr.

The measured coordinate Y0 was used to further subdivide the total solid angle into 9 nearly equal bins each with $\Delta Y0 = 0.5$ cm corresponding to a 0.27° range in the scattering angle Θ. The actual profile for each bin was, in effect, a convolution of this value and a Gaussian function with a width of $\sim 0.15°$ corresponding to the width of the beam spot on the target. This fine binning of the data made the corrections to account for the finite size of the bin negligible. For each of the spectra with the cryogenic target the mean scattering angle was determined with the precision of about 0.02° from the measured energy difference of protons elastically scattered from the aluminum and deuterium nuclei. With the mixed LH_2/LD_2 target the kinematic shift of the $H(p,p_0)$ peak provided confirmation of these estimates. The nominal setting of the MRS angle agreed with that measured for the middle of the 9 bins to within 0.25°. The difference between these values was sensitive to the steering of the incident beam but was essentially the same for all the observations with the same beam tune.

The measurements of σ_{pd}/σ_{pp} with the LH_2/LD_2 mixture were done at each energy with eight nominal settings of the MRS angle: 4, 5, 6, 7.25, 8.5, 9.75, 11 and 12.5°. Since, at each setting, the nine bins in Y0 spanned a total angular range of 2.4°, the substantial overlap provided valuable checks on the consistency of the

results. Each measurement with the LD_2 target required longer running periods performed at the nominal angles of 4, 6, 8.5 and 11°.

By measuring the ratios σ_{pd}/σ_{pp} and $\sigma_{pd'}/\sigma_{pd}$ one avoids the uncertainties resulting from inefficiencies in FEC0 and from possible variations of the exact size of each 0.5 cm bin in Y0. Any slow variations in the acceptance of the MRS with XF or possible local variations in the efficiencies of the VDCs, however, could have influenced the result.

The slow variation in the acceptance with XF was measured by successive runs at different values of the MRS dipole field using the elastic proton peak from the aluminum target. The results, described in detail in the appendix D, spanned a range in XF much larger than was actually used in the experiment. It is concluded that over the limited momentum range sampled in this experiment the slow variation in the acceptance was substantially less than 1%.

The efficiency of proton detection in a localized region of the focal plane depends sensitively on the efficiencies of individual wires in the VDCs. There is inherent redundancy in the data from each VDC plane which arises from the number of adjacent wires normally triggered by a valid event. By a technique described in appendix D this redundancy was exploited to both estimate the efficiencies of individual wires and to recover $\sim 80\%$ of the data that would have been lost because of any inefficiencies. As a direct test of the effectiveness of these techniques the (p,p') continuum at large values of the energy loss ω was examined with the LD_2 target at $E_i = 456.6$ MeV. The results, again presented in appendix D, indicate that the effect of any local variations in the efficiencies of the VDCs is less then 1%.

3. Experimental Results

3.1. THE ELASTIC SCATTERING RATIOS: σ_{pd}/σ_{pp}

Three of the spectra used to determine the ratios of the differential cross sections for the elastic scattering of protons from deuterium and hydrogen at 198.5 MeV are illustrated in fig. 2. In each case the spectrum is one of the nine recorded simultaneously corresponding to equal intervals in the scattering angle $\Delta\Theta = 0.27°$. The data were recorded with the liquid target filled with nearly equal concentrations of deuterium and hydrogen (appendix A). The three prominent peaks (in order of increasing channel number) result from the (p,p_0) reaction on the aluminum windows of the target, the deuterium and the hydrogen. At all angles the very small contributions from the $^{27}Al(p,p')$ reaction were subtracted on the basis of spectra recorded with the pure aluminum target. These corrections were always below 1% and in most cases below 0.5%. In cases such as the spectrum at $\Theta = 6.2°$ the ratio σ_{pd}/σ_{pp} was derived simply from the ratio of the two integrated peak intensities corrected for the $(0.4 \pm 1.0)\%$ difference in the deuterium/hydrogen concentrations.

At the smaller angles, particularly at E_p=198.5 MeV, the three peaks overlapped as illustrated in fig. 2a. Corrections for the contributions of the tails of overlapping peaks were made on the basis of the empirical function chosen to account in detail for the complicated peak shapes as described in appendix C. The fitted shapes used in the analysis at 4.2° are shown in fig. 2a. At the smallest angles not all the parameters in the empirical fits to the individual peaks could be uniquely

determined. In these cases the resulting uncertainties in the areas of the deuterium and hydrogen peaks were estimated and added to the statistical errors.

At the larger angles ($\Theta > 7°$ at 198.5 MeV) the $H(p,p_0)$ peak overlapped with the continuum from the $d(p,p')$ reaction as illustrated in fig. 2c. The continuum was subtracted using spectra measured at the same angle with the pure LD_2 target. The $d(p,p')$ continuum shown in fig. 2c is derived from the LD_2 spectrum suitably shifted and normalized to match the $d(p,p_0)$ peak. Alternatively at the largest angles where the $d(p,p')$ continuum is featureless, it was fitted with a quadratic function which was then used for subtraction. In these cases the two methods of subtraction were found to yield consistent values for the integral of the $H(p,p_0)$ peak. The small uncertainty in the subtraction of the continuum was included in the error estimated for this integral.

The results of the measured ratios σ_{pd}/σ_{pp} are given as a function of the laboratory angle Θ in table 1 for the three proton energies. The 72 spectra recorded with eight different settings of the nominal MRS angle provided substantial overlap. In these regions the measured ratios were consistent within the statistical uncertainties and the closely-spaced pairs of data points resulting from adjacent settings of the nominal MRS angle were averaged. The resulting values at 43 angles for each proton energy are the entries in table 1 and are plotted in fig. 3.

The tabulated errors for the ratios include the statistical uncertainties in the peak integrals together with those attributed to the overlapping peaks at smaller angles and the subtraction of the $d(p,p')$ continuum at larger angles. The precision of the quoted results (in some cases $\pm 0.6\%$) rests in large measure on the technique of measuring the ratio from a single spectrum using the same small angular bin.

There are several sources of systematic uncertainties that are not included in the errors quoted in table 1 or plotted in fig. 3. The most significant of these is attributed to the 1.0% uncertainty in the estimated ratio of the concentrations of deuterium and hydrogen in the target (appendix A). The measurements of the variation of the MRS acceptance with XF outlined in appendix D have been used to estimate that the maximum effect on the results quoted in table 1 is $< 0.5\%$. Combining these errors yields a total systematic uncertainty in the measured values of σ_{pd}/σ_{pp} of $\pm 1.1\%$. As indicated previously (subsect. 2.4) the observed kinematic separation of the three elastic scattering peaks has been used to determine the mean scattering angles for each bin to a precision of $\pm 0.02°$.

3.2. THE $d(p,p')$ SPECTRA

The inelastic proton scattering from deuterium was analysed in terms of the quantity $\sigma_{pd'}(\Theta,\varepsilon)$ defined in eq. (3). The values were measured relative to σ_{pd} at the same angle. The data were derived from spectra recorded with pure LD_2 in the target cell as illustrated in fig. 4. The data in fig. 4. are plotted as a function of $\omega = E_i - E_f$. The spectrum is dominated by the peaks corresponding to the elastic scattering on aluminum and deuterium together with the broad continuum from the $d(p,p')$ reaction. An indication of how small are the contributions from the $H(p,p_0)$ and $Al(p,p')$ reactions is the near absence of events in the interval between the $d(p,p_0)$ peak and the $d(p,p')$ continuum.

The energy calibration of the focal plane was a crucial factor particularly in the detailed analysis of the shape of the $d(p,p')$ at $E_p = 198.5$ MeV which is discussed in

subsect. 5.3. The procedure involving the analysis of $^{12}C(p,p')$ spectra is discussed in detail in appendix B. The transformation of the energy scale to the np excitation energy ε was based on relativistic kinematics. In order to reduce the sensitivity of the results to local variations in the efficiencies of the VDCs, the spectra at E_i = 198.5 MeV were recorded for several (usually six) values of the spectrometer magnetic field. The several spectra corresponding to the same angular bin were added together using the ε calibrations and the well determined locations of the two elastic scattering peaks.

The results of the measurements of the $d(p,p')$ spectra at two angles for each of the three proton incident energies are illustrated in fig. 5. The cross sections have been normalized relative to the deuteron elastic scattering peak observed in the same spectra. The measurements of the σ_{pd}/σ_{pp} described in subsect. 3.1 were then used to relate the $d(p,p')$ spectra to elastic pp scattering at the same angle. Finally the absolute scale on the ordinate in fig. 5 was derived by assuming σ_{pp} is given by the Arndt SM90 phase shifts[17]. The errors include the statistical uncertainty of the data in each energy bin ($\Delta\varepsilon$ = 20 keV), a very small contribution from the corresponding uncertainty in the integral of the $d(p,p_0)$ peak and the statistical uncertainty estimated in table 1 for the ratio σ_{pd}/σ_{pp}. Since all the detailed analysis of the results of this paper is in terms of the cross sections measured relative to σ_{pp} the uncertainty in the elastic pp data is not included.

At each energy (E_i) spectra similar to those illustrated in fig. 5 were derived for 35 angles in the range $2.8° < \Theta < 12.1°$. The dependence of σ_{pd} on two finely-binned variables (Θ and ε) and the sensitivity of the results near the np threshold to the experimental energy response function preclude a simple tabulation of all the data in a form similar to table 1. The most important features of the $d(p,p')$ data are presented in the form of comparisons with detailed predictions based on the IA in subsect. 5.2 and 5.3.

4. Predictions of the Impulse Approximation

The elastic and inelastic scattering cross sections were calculated in the impulse approximation with plane waves in the incoming and outgoing channels. The proton-deuteron scattering amplitudes were constructed from the free NN amplitudes and the form factors representing the structure of the deuteron and final state system. The effects of the reaction dynamics, such as distortions of the incident and exit waves, double scattering and off-shell effects, were neglected. Outlined below is the formalism used in the calculations.

The differential cross section for elastic scattering is expressed by the equation:

$$\sigma_{pd}(\Theta) = \frac{1}{(2J_D+1)(2s_1+1)} \sum_{M_D M'_D m_1 m'_1} |T^{m_1 m'_1}_{M_D M'_D}(\Theta)|^2 \qquad (6)$$

and in the IA[3]) the pd scattering amplitude is:

$$T^{m_1 m'_1}_{M_D M'_D}(\Theta) = t^{(np)m_1 m'_1}_{m_2 m'_2}(\Theta) < \Phi_{J_D M'_D}(\vec{r})\xi_{m'_1} \parallel \exp(i\vec{q}\cdot\vec{r}/2) \parallel \Phi_{J_D M_D}(\vec{r})\xi_{m_1} > + t^{(pp)m_1 m'_1}_{m_2 m'_2}(\Theta) < \Phi_{J_D M'_D}(\vec{r})\xi_{m'_1} \parallel \exp(-i\vec{q}\cdot\vec{r}/2) \parallel \Phi_{J_D M_D}(\vec{r})\xi_{m_1} > \qquad (7)$$

with $\vec{q} = \vec{p_f} - \vec{p_i}$ the momentum transfer to the deuteron. The ξ_m is the spin part of the wave function.

The deuteron wave function is expressed in the form:

$$\Phi_{J_D M_D}(\vec{r}) = \sum_{l_D m_{l_D} m_{s_2} m_{s_3}} < l_D m_{l_D} s_D m_{s_D} | J_D M_D > < s_2 m_{s_2} s_3 m_{s_3} | s_D m_{s_D} > f_{l_D}(r) Y_{l_D m_{l_D}}(\vec{\Omega}_r)\xi_{m_{s_2}}\xi_{m_{s_3}} \qquad (8)$$

In these formulae l_D, s_D and J_D are the orbital angular momentum, spin and total angular momentum of the deuteron. The spins and magnetic quantum numbers of the struck nucleon, the spectator nucleon in the deuteron, and of the energetic proton are s_2, m_2, s_3, m_3, and s_1, m_1 respectively. The quantities of the final state are primed. The $t^{(np)m_1 m'_1}_{m_2 m'_2}(\Theta)$ and $t^{(pp)m_1 m'_1}_{m_2 m'_2}(\Theta)$ are the free neutron-proton and proton-proton scattering amplitudes. In all these formulae Θ is the scattering angle in the laboratory system. $\vec{\Omega}_r$ is defined as $\vec{r}/|\vec{r}|$, where $\vec{r}$ is the relative position vector of two nucleons.

Eq. (6) can be written in the form:

$$\sigma_{pd}(\Theta) = 4\pi(\frac{\hat{s}'_D \hat{J}_D}{\hat{s}_1 \hat{s}_2})^2 \sum_{JM m_1 m'_1} | \sum_{l_D l'_D s m_s} i^l (-)^s \hat{l}\hat{l}_D \hat{s}^2 Y^*_{lm}(\vec{\Omega}_q) F_{l_D l'_D}(q) B^{m_1 m'_1}_{s m_s}(\Theta) W(s s_2 s_D s_3; s_2 s_D) X(l s J, l_D s_D J_D, l'_D s_D J_D) < l_D 0 l 0 | l'_D 0 > < l m s m_s | J M > |^2 \qquad (9)$$

In eq. (8) $\vec{l} = \vec{l'_D} - \vec{l_D}$ is the orbital angular momentum transferred to the deuteron. $\vec{s} = \vec{s'_2} - \vec{s_2}$ is the spin transferred to the struck nucleon which, since the spectator nucleon is not involved in the scattering, is the same as the spin transferred to the deuteron $\vec{s} = \vec{s'_D} - \vec{s_D}$. $\vec{J} = \vec{J'_D} - \vec{J_D}$ is the total angular momentum transfer. W and X are Racah and $9-j$ spin coupling coefficients, and $F_{l_D l'_D}(q) = \int_0^\infty r^2 dr j_l(\frac{qr}{2}) f_{l_D}(r) f_{l'_D}(r)$ is the form factor. The $B^{m_1 m'_1}_{s m_s}(\Theta)$ are irreducible tensors constructed from the NN scattering amplitudes using the formulae presented in appendix E. The standard notation $\hat{s} = \sqrt{2s+1}$ is used.

To calculate the inelastic scattering cross sections the wave functions of the final state are expressed in the following form:

$$\Psi_{J_{np} M_{np}}(\vec{k},\vec{r}) = \sqrt{\frac{2}{\pi}} \sum_{l_{np} m_{l_{np}} m_{s_2} m_{s_3}} < l_{np} m_{l_{np}} s_{np} m_{s_{np}} | J_{np} M_{np} > < s_2 m'_{s_2} s_3 m'_{s_3} | s_{np} m_{s_{np}} > g_{J_{np} l_{np}}(kr) Y^*_{l_{np} m_{l_{np}}}(\vec{\Omega}_r) Y_{l_{np} m_{l_{np}}}(\vec{\Omega}_k)\xi_{m'_{s_2}}\xi_{m'_{s_3}} \qquad (10)$$

Here $g_{J_{np} l_{np}}(kr)$ is the wave function and $J_{np}, M_{np}, l_{np}, m_{l_{np}}, s_{np}$ and $m_{s_{np}}$ are the quantum numbers of the final state unobserved np system. The $\sqrt{\frac{2}{\pi}}$ normalization factor is the same as is used in ref.[18]). With this factor the integral of the $^1S_0$ contribution to the break-up spectrum at small momentum transfers becomes equal

to the cross section obtained from the sum of the NN spin-flip scattering amplitudes for non-interacting target nucleons.

The (p,p') cross sections can then be written in the form:

$$\sigma_{pd'}(\Theta) = \frac{M_N}{2}k(\frac{\hat{s}_D}{\hat{s}_1\hat{s}_2})^2 \sum_{JJ_{np}Mm_1m_1'} | \sum_{l_Dl_{np}sm_s} i^l(-)^s\hat{l}\hat{l}_D\hat{s}_{np}\hat{J}_{np}\hat{s}^2Y^*_{lm}(\vec{\Omega}_q)$$
$$F_{l_DJ_{np}l_{np}}(k,q)B^{m_1m_1'}_{sm_s}(\Theta)W(ss_2s_{np}s_3;s_2s_D)X(lsJ,l_Ds_DJ_D,l_{np}s_{np}J_{np})$$
$$< l_D0l0|l_{np}0 >< lmsm_s|JM > |^2 \qquad (11)$$

where k is the relative momentum of two nucleons in the final unbound state.

The form factor for the break-up cross sections is defined as:

$$F_{l_DJ_{np}l_{np}}(k,q) = \int_0^\infty r^2drj_l(\frac{qr}{2})f_{l_D}(r)g_{J_{np}l_{np}}(kr) \qquad (12)$$

The expressions for σ_{pd} (8) and $\sigma_{pd'}$ (9) represent extensions to all partial waves of the formulation of the IA developed by Cromer[4]). In the limit that the deuteron ground state is pure $^3S_1$ the expressions for the elastic scattering and for the inelastic scattering to the $^1S_0$ continuum are identical. The elastic scattering cross section at small angles is dominated by the spin independent NN scattering amplitude $A(\Theta)$, as the spin dependent amplitudes of the proton-neutron and proton-proton scattering have nearly opposite phases and their sums are small. In the IA the cross section $\sigma_{pd'}$ for the reaction populating the $^1S_0$ scattering state depends only on the spin dependent amplitudes C(Θ), M(Θ), G(Θ) and H(Θ).

The deuteron wave function and the final state wave functions were calculated from the Paris potential[19]). Since the Paris potential does not include terms breaking isospin symmetry the strength of the spin-singlet, isovector part of the potential had to be adjusted to reproduce the scattering length a_{np}. To reproduce exactly a_{np} known from low energy experiments the $V_{S=0,T=1}$ potential was scaled by the factor 1.043. The sums over l, J_{np} and l_{np} in equations 8 and 9 extended up to three. Contributions from the higher orbital angular momentum transfers, and higher final spins were negligibly small because of the small values of q and k. As evidence of this, at 198.5 MeV the contribution from the final states with $l_{np} = 3$, in the excitation range below 5 MeV, is calculated to be lower than 1% of the total yield.

5. Comparison of Data with IA Predictions

5.1. ELASTIC SCATTERING RATIOS σ_{pd}/σ_{pp}

The measured ratios σ_{pd}/σ_{pp} are compared in fig. 3 with two predictions of this quantity based on the IA in the form presented in sect. 4. The solid curves are based on the intermediate energy NN scattering amplitudes (at E_i=198.5, 297.6 and 456.6 MeV) fitted by Arndt *et al.* and designated SM90 in the computer program SAID[17]). The dashed curves result from the amplitudes listed in the same program but derived using the Bonn potential[20]). In both cases the deuteron wave function was that derived using the Paris potential[19]). In the lower panels of fig. 3 the corresponding predictions of σ_{pp} and σ_{pd} are shown separately. These panels illustrate the strong influence of the Coulomb interaction at the smallest scattering angles and the extent

to which some of the differences between the two sets of NN amplitudes cancel in predicting the ratio σ_{pd}/σ_{pp}. It should be emphasized that the comparisons between data and the predictions based on the simple IA shown in the upper panels of fig. 3 involve no arbitrary parameters or normalization.

A more detailed comparison between the extensive data given in table 1 and predictions based on several different sets of NN amplitudes is presented in fig. 6. The data points in this figure represent the measured ratio σ_{pd}/σ_{pp} divided by the ratio σ_{pd}/σ_{pp} predicted using the SM90 amplitudes. Comparisons of the data are also made with the predictions based on other intermediate energy NN amplitudes; specifically FA91, V350 and the local phase shift solutions of Arndt, and of the Bonn and Paris potentials. In each case the curves are calculated using the amplitudes listed in SAID and dividing the predicted ratio σ_{pd}/σ_{pp} by the corresponding ratio predicted using SM90. It is evident from both fig. 3 and fig. 6 that, at E_i = 198.5 MeV the data for angles $\Theta > 5°$ lie consistently below the predictions of the IA. At the higher energies the data are typically within 5% of the predictions over the complete angular range. It should be noted that at these higher energies the ratios σ_{pd}/σ_{pp} predicted using the Saclay and BASQUE phase shift solutions tabulated in SAID differ from the data by substantially more than the predictions included in fig. 6. The influence of the bound state wave function was also investigated. The values of σ_{pd} predicted using the Bonn potentials A, B and C[20]) differed from these obtained with the Paris wave function by < 2%. Further discussion of these results is deferred to subsect. 6.1.

5.2. DEUTERON INELASTIC SCATTERING: $\sigma_{pd'}/\sigma_{pp}$

Adopting the formalism outlined in sect. 4, the value of $\sigma_{pd'}(\Theta,\varepsilon)$ can also be predicted in the IA from the NN amplitudes at intermediate-energies and a model of the low-energy NN interaction which defines the properties of the deuteron and the low energy np phase shifts. The results of such calculations fitted to the experimental data using one normalization parameter for each spectrum are shown in fig. 5. The detailed shapes of predictions shown are based on eq. (9) using the SM90 NN amplitudes and the Paris potential modified slightly as discussed in sect. 4 to reproduce exactly the known $^1S_0$ scattering length a_{np}. The theoretical predictions have been convoluted with the experimentally measured shape of the deuteron elastic scattering peak. The convolution of the experimental response function is of crucial importance to the analysis of the break-up spectra near the np threshold. At the smaller angles the procedure referred to in subsect. 3.1 and discussed in detail in appendix C was used to subtract the tail of the Al(p,p_0) peak from the measured shape of the $d(p,p_0)$ peak. The subtraction of the tail of the elastic peak from aluminum also permitted an accurate estimate of the integral of the $d(p,p_0)$ peak in each spectrum. This integral together with the measured ratios σ_{pd}/σ_{pp} allowed the measured intensity in each energy interval of the $d(p,p')$ spectra to be related to σ_{pp} at the same scattering angle.

The single free parameter used in each fit to the data shown in fig. 5 is a normalization of the predicted spectrum at each angle. This parameter is fitted on the basis of the data in the interval $\varepsilon \leq 3.9$ MeV. The same IA calculations used to predict the shapes of the spectra have also been used to predict $\sigma_{pd'}/\sigma_{pp}$. In fig. 7 is plotted the amount by which the empirical normalization of the data differs from

the normalization predicted in the IA with the SM90 amplitudes. The errors shown for the experimental points include those arising from the statistical precision of the (p,p') spectra, the uncertainty in the integral of the $d(p,p_0)$ peak, the error of the ratio σ_{pd}/σ_{pp} obtained from table 1 and an uncertainty of between 1 and 2% which is the variation that would result if the upper limit of the value of ε used to define the region of the fit were varied in the range from 2.9 to 4.9 MeV. As is the case in fig. 6 for σ_{pd}/σ_{pp}, the experimentally determined ratios $\sigma_{pd'}/\sigma_{pp}$ are also compared with predictions in the IA using other NN amplitudes. This is achieved by also comparing in fig. 7 the values of $\int_{\varepsilon=2.2}^{3.9\mathrm{MeV}} \sigma_{pd'}(\varepsilon)d\varepsilon/\sigma_{pp}$ for these amplitudes with the values derived with the SM90 amplitudes.

The break-up spectra just above the threshold are dominated by the $^1S_0(d^*)$ resonance particularly at the smallest values of the momentum transfer q. This result is illustrated by the IA predictions shown in fig. 5. The contributions to the total spectra from all final states except the $^1S_0$ is the smooth lower curve in each segment of the figure. The generally excellent agreement between the predicted shapes of the (p,p') spectra and the data presented in fig. 5 indicates that the IA accounts very well for the relative contributions of the $^1S_0$ and all other final states. An analysis of the success of the IA in predictions of the detailed shape of the $^1S_0$ resonance at $E_p = 198.5$ MeV is included in subsect. 5.3.

The observed strength of the Gamow-Teller transition between the deuteron ground state ($1^+, T = 0$) and the d^* resonance ($0^+, T = 1$) has been estimated by subtracting the component given by the lower curves shown in fig. 5. The high energy tail of the d^* resonance extends well beyond both $\varepsilon = 3.9$ MeV, the upper limit of the data included in the fit to the IA, and the maximum energy of the data analysed in this experiment. The fitted shapes predicted by IA were therefore used to estimate $\sigma_{pd^*}(\Theta)$, the integral of the $^1S_0$ cross section over all values of ε. The resulting values of the ratio $\sigma_{pd^*}/\sigma_{pp}$ are listed in table 2 and plotted in fig. 8. In addition to the uncertainty assigned to the ratio $\sigma_{pd'}/\sigma_{pp}$ the errors quoted in table 2 include the variation that would result from a $\pm 5\%$ change in the relative contribution of all the final states except the d^* in the range $\varepsilon \leq 3.9$ MeV. This uncertainty becomes a dominant component at large values of the momentum transfer.

The values of $\sigma_{pd^*}/\sigma_{pp}$ derived from the present experiment are plotted in fig. 8. Also shown in this figure are the corresponding ratios predicted using the IA on the basis of the SM90 and Bonn NN amplitudes. As in fig. 3 for the ratio σ_{pd}/σ_{pp}, the lower panels in fig. 8 show the dependence on Θ of the predicted values of σ_{pd^*} and σ_{pp} separately.

5.3. THE (p,p') DATA AND a_{np} AT $E_i = 198.5$ MeV

At $E_i = 198.5$ MeV the $d(p,p')$ data were recorded with a precision intended to provide a critical test of the sensitivity of the shape of the d^* resonance to the value of a_{np}, the $^1S_0$ scattering length. In this section the analysis is in terms of the IA as expressed in eq. (9) with the NN amplitudes given by the SM90 solution.

As in subsect. 5.2, the initial analysis assumes a final state interaction defined by the Paris potential modified to reproduce the value $a_{np} = -23.748 \pm 0.009$ fm derived from the analysis of low-energy np scattering[14]). The sensitivity of the result to the tail of the $A(p,p_0)$ peak is discussed in appendix C. At angles $\Theta < 3.82°$ it

was concluded that the uncertainty in the $d(p,p_0)$ lineshape precluded a meaningful analysis of the (p,p') data in terms of a_{np}.

The measured and calculated break-up spectra for three scattering angles 4.08, 6.50 and 9.09° are compared in fig. 9. For each of the solid curves, the only free parameter is the overall normalization of the spectrum which is determined by a fit to the data in the region $\varepsilon < 3.9$ MeV. The location of the np threshold ($\varepsilon = 2.2245$ MeV) is fixed by $\varepsilon = 0$, the observed location of the $d(p,p_0)$ peak and the measured energy calibration of the spectrometer (appendix B). The difference between the individual data points and the solid curves are plotted in the lower segment of each figure. The quality of the fit for each of the three spectra in fig. 9 is defined by the values of χ^2_1 and the degrees of freedom shown in the upper third of table 3.

In order to asses the sensitivity of the $d(p,p')$ spectra to the value of a_{np}, separate calculations of $\sigma_{pd'}$ were also made using the strength of the $V_{S=0,T=1}$ component of the Paris potential adjusted to give a_{np}=-22, -24 and -26 fm. Over this limited range each value of $\sigma_{pd'}$ was expressed as a quadratic function of the "parameter" a_{np}. On this basis a second fit was made to each of the observed spectra in which both the normalization and a_{np} were free parameters. Although these two-parameter fits are also shown in fig. 9 the best indication of the improvements in the quality of the fits are the values of χ^2_2 listed in the middle section of table 3. As is indicated in this table substantially improved fits are obtained at each angle with values of a_{np} more negative than the accepted value. The statistical errors of the fitted values of a_{np} listed in table 3 correspond to the limits for which χ^2 would be increased by 1 from its quoted minimum value. The potential systematic errors in this analysis are discussed below.

The one and two-parameter fits referred to above rely on a calibration of ε defined by the location of the $d(p,p_0)$ peak and precise measurement of the dispersion of the spectrometer. As a result of the analysis outlined in appendix B it is estimated that the uncertainty in this dispersion corresponds to a ± 1.0 keV uncertainty in the calibration in the region of the np threshold. As a test of the sensitivity of the results to this estimate, a third set of fits was made in which the location of the threshold was also a free parameter defined in terms of $\Delta\varepsilon = \varepsilon_{th}(\text{fitted}) - 2.2245$ MeV. The results of these 3-parameter fits to the spectra in fig. 9 are summarized in the lower section of table 3. In sharp contrast to the improvement in the fits achieved by making a_{np} a parameter, no substantial reduction in χ^2 results from the use of a fitted $\Delta\varepsilon$. Moreover, because of the strong correlation between a_{np} and $\Delta\varepsilon$ the statistical uncertainty in a_{np} is substantially increased.

The procedure outlined above was carried out for each of the spectra recorded in the angular range from 4° to 12°. In addition, for each spectrum the influence of the range of excitation energies included in the fit was investigated by adopting three different upper limits $\varepsilon < 2.9, 3.9$ and 4.9 MeV. All the results for the fitted values of a_{np} are shown in fig. 10. Several of the spectra recorded at $\Theta_{\mathrm{MHS}} = 11°$ were contaminated in the region $\varepsilon > 2.9$ MeV by the presence of the $H(p,p_0)$ peak resulting from the use of the lower purity deuterium at this angle. In these cases the absence of values plotted in fig. 10 indicates that no fits to a_{np} were attempted. Although the high purity deuterium (> 99.99%) was used at $\Theta_{\mathrm{MHS}} = 4$ and 8° the erratic behaviour of the fits at 7.49, 7.76, 8.02 and 8.29° is also attributed to the presence of a very weak $H(p,p_0)$ peak located in the region most critical to the measurements of

a_{np} ($\varepsilon \sim 2.3$ MeV). The points plotted in this region illustrate the value of making the measurements of a_{np} over a wide range of conditions and the use of the fit with a variable $\Delta\varepsilon$ as a diagnostic. The fits at these four angles were not included in further analysis. The H(p,p_0) peak seen at $\Theta_{MHS} = 4$ and 8° represented a 0.1% contamination of the LD_2 target and was attributed to vapors containing hydrogen frozen on the windows of the cryogenic target.

The results obtained from this analysis of $\sigma_{pd'}$ in terms of a_{np} are essentially insensitive to the particular choice of the intermediate energy NN amplitudes. In eq. (9) the dependence of $\sigma_{pd'}$ on k (or equivalently ε) is defined by the form factor $F_{ll_D J_{np} l_{np}}(k,q)$ given in eq. (10) For small values of k and q the shape of $\sigma_{pd'}(\varepsilon)$ is essentially determined by $F_{0000}(k,q)$, the form factor for the $^3S_1 \rightarrow {}^1S_0$ transition. The contributions arising from all values of $J_{np} \neq 0$ are shown separately in fig. 9. If one used a set of NN amplitudes other than SM90 the effect would be a very small change in the relative amplitude of the $J_{np} \neq 0$ contributions.

The sensitivity of the results obtained in this section to the shape of the NN potential at low energies has been investigated using the effective range formalism (1). The Paris potential used to calculate the final state wave functions predicts a value of the $^1S_0$ effective range $r_e = 2.88$ fm, whereas the recommended value is 2.75 ± 0.05 fm[8]). The correlation between the fitted values of a_{np} and r_e was estimated using a square well potential. In the analysis of the data with $\varepsilon < 4.9$ MeV a reduction in the effective range by 0.1 fm would change the fitted value of a_{np} by -0.1 fm. For the fit to the data with $\varepsilon < 3.9$ MeV the corresponding change is Δa_{np}= -0.05 fm, and for $\varepsilon < 2.9$ MeV the effect is negligible.

The fits to a_{np} at different angles were independent, and since in many cases the statistical precision of a fit was better than 0.3 fm (with $\Delta\varepsilon = 0$) it is evident that systematic uncertainties played a dominant role. The most obvious of these is the effect of the ± 1.0 keV precision estimated in appendix B for the calibration used to locate the np threshold relative to $\varepsilon = 0$. As noted earlier, the fitted value of a_{np} is strongly correlated with this quantity and a 1 keV shift changes a_{np} by typically 0.27 fm. The effect of small differences in the experimental lineshape at $\varepsilon \sim 2.3$ MeV compared to the measured response at $\varepsilon = 0$ has also been investigated. A 3% change of the width parameter w (appendix B) would alter the fits with $\varepsilon < 3.9$ MeV by 1 fm and those with $\varepsilon < 2.9$ MeV by 2 fm. Direct measurements of the change in w for different locations of the $d(p,p_0)$ peak on the focal plane, for the different values of E_t and consideration of the known variation of the dE/dx with E_f indicate that a reasonable upper limit on the change in w at $\varepsilon = 2.3$ MeV is 0.6%. At this limit the change in a_{np} is 0.2 fm for $\varepsilon < 3.9$ MeV and 0.4 fm for $\varepsilon < 2.9$ MeV. Further discussion of the results presented in fig. 10 is deferred to subsect. 6.3.

6. Discussion

6.1. σ_{pd}/σ_{pp}

The results of the present experiment to measure the elastic scattering ratios σ_{pd}/σ_{pp} for the three energies and in the angular range $3° \leq \Theta \leq 14°$ are presented in different forms in fig. 3, fig. 6 and table 1. The errors presented for each value of the ratio are generally $\leq 1\%$ for $\Theta > 4°$ and account for all the known uncertainties in the experiment except for the overall systematic error estimated to be $\pm 1.1\%$ which is

dominated by the uncertainty in the ratio of hydrogen and deuterium concentrations in the LH_2/LD_2 target. The results in fig. 3 and fig. 6 are presented in the form of comparisons with predictions of the IA described in sect. 4. These comparisons are made knowing that the IA is certainly an incomplete theory and that as far as the reaction mechanism is concerned the interesting physics lies "beyond" this simple model.

A general conclusion that can be drawn from fig. 6 is that under these restricted experimental conditions the net effect of the physics beyond the simple model is modest. At 198.5 MeV and all but the smallest angles the experimental ratios are typically 10 to 15% below the predictions of the IA. The agreement at the higher energies is even better and the systematic deviations of the data from any of the predictions are of the same magnitude as the differences in the IA that result from the use of various NN amplitudes. Empirically it appears that in the TRIUMF energy range the net correction to the IA varies smoothly with E_t and changes sign. Without invoking a model of the expected corrections to the IA one should not use the comparison between the data and individual predictions in fig. 6 to draw conclusions with regard to the validity of any specific formulation of the NN amplitudes. The quality of the data and the observation that the sums of all corrections are modest suggest that if the size of these corrections can be predicted to within 10% meaningful conclusions in this regard can be drawn on the basis of the existing data.

The original data on σ_{pd} at $E_t = 158$ MeV[5]) was also compared with the predictions of the IA. Although it is difficult to make detailed comparisons with the data at 198.5 MeV presented in fig. 6, a similarity is noted. At the smallest angles the data at 158 MeV agreed with or exceeded predictions but at $\Theta = 15°$ the data was lower than the prediction by 15-20%. Surprisingly, there is no other high precision data on pd elastic scattering at small q suitable for comparison with the present results in the TRIUMF energy range.

There are, however, several extensive studies of σ_{pd} at scattering angles $\Theta < 14°$ in the energy range from 582 to 991 MeV[21-24]). In all these experiments the recoil deuteron was detected with the intention of excluding possible contributions from inelastic scattering. Only in the case of the data at 582 MeV[21]) are there results reported for σ_{pp} recorded in the same experiment. In this case the measured ratio σ_{pd}/σ_{pp} at $\Theta = 12°$ is consistent with the ratio predicted in the IA (8) using the NN amplitudes of SM90 within the experimental accuracy of $\sim \pm 8\%$. All of the data at higher energies[22-24]) have been compared with predictions that include the effects of multiple scattering. Good agreement is observed. In particular the more recent data at 793 MeV[24]) appear to be in excellent agreement with both the data of Irom *et al.*[23]) at 796 MeV and calculations including double scattering following the prescription of Alberi *et al.*[25,26])

6.2. $\sigma_{pd'}/\sigma_{pp}$, $\sigma_{pd^*}/\sigma_{pp}$

Fig. 5 illustrates good agreement between the measured shapes of the $d(p,p')$ spectra and the predictions based on the IA. In particular the relative contribution of the d^* and the sum of all the other states of the unobserved np system seems to be adequately accounted for over the limited range in momentum transfer and excitation energy sampled in this experiment. This agreement makes meaningful a comparison in fig. 7 of the amount by which the predictions of the IA must be scaled to match

each experimental spectrum.

Generally the comparisons between the data and the predictions of the IA for the deuteron inelastic scattering (fig. 7) are very similar to those discussed in Sec 6.1 for the $d(p,p_0)$ reaction (fig. 5). At $E_i = 198.5$ MeV the data for $\Theta > 4°$ lie 5 to 15% below the predictions. Once again the discrepancies appear to change sign or become smaller in magnitude at the higher proton energies. A very consistent picture emerges of data determined with a precision of 1-2% differing from the very simple predictions by typically 10%. These data therefore provide a firm basis for a proper evaluation of the physics beyond the simple model.

A quantitative treatment of the refinements to the IA is beyond the scope of this paper. The 198.5 MeV data is the object of a rigorous three-body calculation using realistic NN forces[13]). This calculation is valid only below the pion production threshold and does not include the Coulomb interaction[12]). The apparent success of models for σ_{pd} including the effects of double scattering at $\sim$ 800 MeV is noted in subsect. 6.1 Similar calculations are under way to investigate whether such a model can account for the small corrections needed to describe the present data at all three energies. It should be noted that analyses of pd elastic[27]) and inelastic[18]) scattering in a relativistic framework suggest that these effects are small in the kinematic regime sampled by the present data.

The experimental results presented in fig. 8 and table 2 summarize the information derived regarding the strength of the transition to the d^* ($^1S_0$) final state. This transition is uniquely $\Delta S = 1, \Delta T = 1$ and consequently depends on a very different combination of the NN amplitudes than that involved in σ_{pd} [ref.[4])]. These data are the most precise available for this, the simplest pure Gamow-Teller transition for which very detailed models exist of both the initial and final nuclear states. Fig. 8 illustrates the sensitivity of the predictions of the IA for two different sets of the NN amplitudes.

Recently there has been considerable interest in using the (d, ^{2}He) reaction (where the two protons are in the $^1S_0$ state) as a probe of nuclear structure[28]). The adequacy of the IA in describing the σ_{pd^*} data is directly related to similar models[29,18]) used to analyse the data[28,30]) for the elementary process $p(d,\ ^2\mathrm{He})n$. In this connection the previous data most directly comparable to those presented in this paper are those of Kox *et al.*[30]) at $E_d = 350$ MeV which have been compared with the predictions of Carbonell *et al.*[18]). Within the quoted experimental uncertainty of 20% the measured differential cross sections agreed with the predictions over a range in kinematic variables q and ε wider than that sampled in the present experiment.

6.3. σ_{pd^*} AT E_i=198.5 MeV AND a_{np}

A detailed analysis of the shape of the $d(p,p')$ spectra at E_i=198.5 MeV near the np threshold reveals a small but consistent deviation between the data and predictions based on the IA (fig. 9, table 3). It has been empirically determined that one can account for these deviations almost completely by adjusting the strength of the final state np interaction in the $S = 0, T = 1$ channel. The changes can be expressed in terms of values of the $^1S_0$ scattering length slightly different from the value $a_{np} = -23.748 \pm 0.009$ fm derived from low energy np scattering. The data in each angular bin have been used to provide independent estimates of a_{np} as indicated in table 3

and illustrated in fig. 10. It should be noticed that a 1 fm change in a_{np} results from a 0.5 % change in the strength of $V_{S=0,T=1}$.

Because of the sensitivity of the derived values of a_{np} to the energy calibration of the spectra independent analyses was performed with the calibration as a fitted parameter free to assume different values for each angular bin. The main conclusion for this unrealistically relaxed analysis is that the results would appear to confirm the estimate that the calibration at $\varepsilon = 2224.5$ keV is accurate to the estimated precision of ± 1.0 keV. This independent analysis also had the benefit of helping to reveal the presence of a very weak contamination of the $d(p,p')$ spectra from pp elastic scattering.

As indicated previously, a proper analysis of the small deviations between the predictions of the IA and the data illustrated in fig. 10 must include a more complete model. Such a model would presumably account for a possible dependence on Θ of the value of a_{np} fitted on the basis of the IA. Empirically it is observed in fig. 10 that the fitted values are almost independent of Θ over the measured range. Consequently the independent estimates at each angle have been averaged (ignoring the four angles near $\Theta = 8°$) and the results are presented in fig. 11 plotted as a function of the maximum value of ε included in the fit to the (p,p') spectra. It should be noted that although the analysis presented in appendix C indicates that at $\Theta = 3.82°$ the shape of the $d(p,p_0)$ spectrum is most sensitive to the subtraction of the tail of the Al(p,p_0) peak, the fitted values of a_{np} at this angle are completely consistent with the values at larger angles.

It is evident from the analysis presented in subsect. 5.3 that systematic errors will dominate any average of the "empirical" values of a_{np} to be derived from this experiment. The cross-hatched region shown in fig. 11 corresponds to $a_{np} = -24.7 \pm 0.4$ fm. The central value corresponds exactly to the fitted average with the calibration fixed and either $\varepsilon < 2.9$ or $\varepsilon < 3.9$. The largest known systematic error in the estimate of a_{np} with fixed calibration is ± 0.27 fm which arises from the ± 1.0 keV uncertainty in the calibration. In fig. 11 this estimate has been increased by a conservative factor 1.5 to account for possible systematic errors associated with the use of the shape of the $d(p,p_0)$ peak in convoluting the theoretical predictions and the uncertainty associated with contributions to the spectra of final states other than the d^*. The differences between the empirical fits to a_{np} and the value -23.748 $\pm$ 0.009 fm represents a challenge to more complete theories such as the Faddeev calculations currently in progress[13]).

The present results would be relevant to the interpretation of data from the $d(n,p)2n$ reaction at intermediate energies to determine the value of a_{nn}. The fact that the simple IA does not account for our $d(p,p')$ data precludes the use of the reaction $d(n,p)nn$ at 200 MeV to extract a_{nn} until we understand the origin of the IA failure. It is important to keep in mind that the two processes $d(n,p)nn$ and $d(p,p')np$ even at these relatively high energies differ at small angles because of the presence of the Coulomb force. If these theoretical challenges can be met, a measurement of a_{nn} using this reaction at a neutron energy in the vicinity of 200 MeV should be seriously considered. The experimental challenges that would be posed by such an undertaking are formidable, particularly that of obtaining the best possible resolution in the excitation energy ε.

7. Conclusions

The most important consequence of the present experiment is that high precision data now exist for the elastic scattering of protons from deuterium at three energies (198.5, 297.6 and 456.6 MeV) in the forward directions ($\Theta_{lab} < 14°$) and under the same conditions for inelastic scattering involving low excitation energies ($\varepsilon < 5$ MeV) in the unobserved np system. These data must be amongst the most amenable to theoretical predictions because they involve simple nuclear reactions at low q and ε, minimally-interacting nucleons, and the lightest nuclear target for which both the initial and final states are well-known. Much of the data are presented in their most precise form (typically $\pm 2\%$) as ratios of the differential cross sections for elastic and inelastic scattering measured relative to the pp scattering. Detailed measurements of the shape of the $d(p,p')$ continuum are related to the strength of the $^1S_0$ final state interaction.

Predictions of the measured quantities based on the impulse approximation provide an excellent reference for the presentation of these data. This very simple model has been developed in sufficient detail to accommodate various models of the initial and final nuclear states as well as a wide range of the intermediate energy NN amplitudes. The general level of agreement between these predictions and the data is typically 10%.

The shape of the $d(p,p')$ spectrum has been investigated with the greatest precision at $E_i = 198.5$ MeV. At low values of the excitation energy (ε) this shape is particularly sensitive to the final-state interaction in the $^1S_0$ channel. If the model of this interaction is adjusted to exactly reproduce the known value of a_{np}, the $^1S_0$ scattering length, the IA provides reasonable predictions of the measured shape. A significant improvement in the quality of these fits, however, can be obtained empirically by increasing the strength of the final state interaction by $(0.5 \pm 0.2)\%$ in the $S = 0, T = 1$ channel which would correspond to a value of $a_{np} = -24.7 \pm 0.4$ fm.

The data that is presented is sufficiently precise to be sensitive to the physics beyond the simple IA and therefore represents a significant challenge to more detailed theoretical models. If there is significant progress in this regard, then these data possibly augmented by future measurements with greater precision or of other variables could have a significant impact on our understanding of the basic NN interaction. In particular the data exhibit a sensitivity to the intermediate-energy isoscalar NN amplitudes and, as mentioned above, to the low energy scattering length a_{np}. In this regard an adequate theoretical model would be needed to justify new measurements of the neutron-neutron scattering length, a_{nn}, using the $d(\pi,p)2n$ reaction in the intermediate energy region.

Appendix A. LH_2/LD_2 target

The LH_2/LD_2 target was produced by liquefying a gas mixture which had been prepared very carefully to make sure that it contained equal concentrations of both gases. The gases (0.99999 pure H_2 from ®Linde and 0.999 pure D_2 from ®Isotec) were transferred from high pressure supply bottles to two 3 liter sample cylinders. Initially 400 kPa of the H_2 gas was loaded to one cylinder and 400 kPa of D_2 to the other. The pressure difference between the cylinders was measured with a mercury manometer and did not exceed 1 kPa. In the second step 400 kPa of hydrogen was added to the cylinder with deuterium and vice-versa. The final pressures in both cylinders were 800 kPa, and again they were equal within 1 kPa. Small differences in the volumes of the two cylinders and in the pressures added in each step canceled in the first approximation, and hence the total concentrations of the hydrogen and deuterium gases in the two cylinders were very close to equal. After the filling, the two cylinders were left for 6 days to allow the gases to mix. Since the mean path length of the particles in this time was a factor of 15 greater than the height of the cylinders, mixing was nearly complete. This was verified by a Monte-Carlo simulation code. The gas for liquification in the target was taken simultaneously from both cylinders. Owing to the very symmetric procedure of mixing the gases the numbers of deuterium and hydrogen atoms in the mixture were determined to be equal, within an error generously estimated to be < 1%. This ratio in the liquid was slightly different due to the difference in the fractional vapour pressures of the two gases in the filling and safety tubes above the target. The final number for the D/H concentrations in the target cell was 1.004 ± 0.010.

Because of the importance of this parameter it was checked in two independent ways. Mass spectroscopy analyses of two gas samples taken during the filling provided a D/H ratio 0.955 ± 0.03, which would correspond to a ratio of 0.96 ± 0.03 in the liquid. The other method of checking the ratio of D/H concentrations in the target consisted of comparison of the ratios of elastic scattering peaks from runs with the LH_2/LD_2 target, as well as with the same target filled with pure LD_2 and pure LH_2. The ratio of the number of counts in the peak from scattering on the hydrogen isotope to the peak from the scattering on the aluminum windows provided a direct measure of the amount of this isotope in the target. The analysis was done using 198.5 MeV data at 6°, where the three scattering peaks were separated, and at 11°, where the deuterium break-up continuum under the hydrogen peak was smooth. The measured D/H ratios were 1.022 ± 0.044 and 1.040 ± 0.044, and their average deviates by 2.7% from the expected value 1.004. The method of peak ratios determined the D/H atomic ratio directly in the target, and its result provides an important independent confirmation of the absolute normalization of our data with 4% accuracy.

The ratio of the peaks from the proton scattering on deuterium and hydrogen atoms was measured several times through the run at $E_i = 198.5$ MeV and $\Theta = 6°$ to monitor possible changes of the target composition. All the results, including the one obtained at the end of the measurements, after the runs at 297.6 and 456.7 MeV, were consistent within a statistical error of 0.75%, confirming that the D/H atomic ratio in the target did not change in time. As a final check the number of counts from scattering on the hydrogen atoms from the water and oil vapour deposited on the cryogenic target was measured immediately after emptying the target. Less than

0.25% of the counts in the scattering peak from hydrogen with the LH_2 target could be attributed to these contaminants.

Although the two measurements of the ratio of D/H concentrations in LH_2/LD_2 mixture are less precise than the estimate based on the filling procedure the three values are mutually consistent. The adopted value of this ratio is 1.004 ± 0.010.

Appendix B. Energy calibration

The energy calibration of the focal plane (XF) was determined using the elastic and inelastic peaks from the scattering of the 198.5 MeV beam on a 25.3 mg/cm^2 thick carbon target. The four peaks corresponding to the energy levels in ^{12}C at excitations 0.0, 4438.9 $\pm$ 0.31, 7654.2 $\pm$ 0.15 and 15110 $\pm$ 3.0 keV were used. The measurements were done at $\Theta \sim 6°$ where the yields from the first and second excited states are about equal. The yield from the ground state transition was reduced to match the yields from the two first excited states by pre-scaling this peak by a factor of 1000. The pre-scaling was realized in the trigger using pulses from a thin scintillator positioned in the focal plane such that only elastically scattered particles were passing through it. To reduce the counting rate, only the part of the focal plane corresponding to excitations up to $\sim$ 8 MeV was activated by including in the trigger only those wires from the corresponding region of the VDC X1. Particles from higher excitations were registered with very small efficiency, only by accidental coincidences in the trigger. The cross section for the state at 15110 keV was so large that the number of counts in this peak was only ten times smaller than the number of counts in the three main peaks. The peak corresponding to this state supplied useful data for a consistency test of the calibration, because of its large distance from the ground state peak. The width of the peaks from the inelastic scattering was $\sim$ 90 keV, but the elastic scattering peak was broadened to about 105 keV by the pre-scaling scintillator situated in front of the VDC chambers.

The positions of the peaks were measured for several magnetic fields of the spectrometer. In the three measurements of the calibration curve done during the experiment the numbers of different values of the magnetic field (N_M) were 17, 12 and 9. The positions of the peaks were calculated by a program fitting their shapes with a formula assuming a Gaussian form close to the centre, and asymmetric tails. The peak positions were determined by the central, Gaussian parts. Uncertainties of the positions, calculated from the correlation matrix of fitted parameters, were of $\sim$ 0.7 keV for the main peaks and 2 keV for the fourth peak. The peak at 7654 keV overlapped with the continuum resulting from the decay of ^{12}C into three α particles above 7280 keV. This continuum was included in the fit, with its shape given by the penetrability of α particles through the Coulomb barrier. In the central region of the 7654 keV peak the continuum was strongly suppressed by the barrier and hence its impact on the peak position was very small. The angular distribution of the scattering to the first excited state was dramatically different from the distributions to all the other states. This produced a small shift of this peak relative to other peaks, which resulted from an imperfect compensation for dependence of XF on the scattering angle. This shift was introduced as a free parameter in fitting the peak positions, and the value of $\sim$ 3 keV obtained from the fits agreed with the estimate of the change of the XF position with the angle.

The $3N_M$ positions of the peaks (excluding the 15110 keV peak) obtained for N_M magnetic field values were fitted with $N_M + 3$ parameters including: three parameters defining quadratic dependence of XF on the proton momenta (p), $N_M - 1$ values of the magnetic field, and the one parameter correcting the position of the peak corresponding to the first excited state. The proton momenta were calculated from kinematics including energy losses in the target, which changed slightly with the proton energy. The values of the magnetic fields obtained from the fit were different from the read-outs of the NMR probe by less than 0.04% which corresponds to an energy difference of about 180 keV.

The χ^2 per degree of freedom obtained from the fit for the three calibration curves were 5.72, 6.75 and 3.50 indicating that the $XF(p)$ dependence was more complicated than quadratic. In fact the results of the first, most precise, measurements of the calibration curve shown in fig. 12 indicate systematic deviations $\Delta\omega$ of the points from the fitted curve of the order of 1 keV. The data are not precise enough, however, to determine a more complicated dependence of the XF position on proton momentum. Possible fluctuations of the true calibration curve around the calculated curve, suggested by the data, should not change the energy difference of two points separated by 2 MeV by more than 1 keV. Because the $d(p,p')$ spectra were measured at several positions on the focal plane, and added together after transformation to the deuteron excitation energy, these deviations were in large part averaged out. The slopes of the three calibration curves measured in the course of the experiment were consistent within 0.4 keV for an interval Δ XF corresponding to $\Delta\omega = 1$ MeV. The error in the distance between the elastic scattering peak and the threshold of the break-up spectra for deuterium target determined using this calibration is estimated to be < 1.0 keV.

Appendix C. Energy response

At small angles the peaks from scattering on deuterium, hydrogen and aluminum nuclei in the target overlapped and were separated using a program which fitted the spectra. In the spectra measured with the LH_2/LD_2 target three peaks, and in the spectra from the LD_2 target two peaks had to be separated. The separation of the peaks measured with the deuterium target was more demanding, as not only the integral of the peak from scattering on deuterium had to be determined, but also its shape.

The asymmetric shapes of the peaks were described by a formula different for the two sides of the peak, but converging to the same, Gaussian form at the centre. The right side of the peak (smaller momenta, larger excitations) was parameterized in the following way:

$$P(x) = h \exp\left(- \frac{(x - x_0)^2}{w^2 + b_R(x - x_0) + c_R(x - x_0)^{1.3}} \right) \left(1 + h_R \left(\frac{\pi}{2} + \operatorname{atan}\left(\frac{x - x_R}{w_R} \right) \right) \right) \tag{C.1}$$

The formula used for the left side was:

$$P(x) = h \exp\left(- \frac{(x - x_0)^2}{w^2 + b_L|x - x_0| + c_L|x - x_0|^{1.3}} \right) \tag{C.2}$$

The parameters h (height), x_0 (position) and w (width) defined the Gaussian shape, and all the other parameters described the shapes of the tails. The last factor in eq. (C.1) was necessary to reproduce the shape of the low energy tail of the peaks as illustrated in fig. 13.

The parameterization of the peaks was determined using the spectra measured with the deuterium target around 6°, where the two peaks from scattering on the aluminum and deuterium nuclei were well separated and measured with high statistical accuracy. The shapes of the peaks were reproduced very well, and the spectra with a very large number of counts were fitted with a χ^2 per degree of freedom of between one and two. The procedure of fitting the spectra was also tested using the well separated peaks from scattering on aluminum and hydrogen, measured with the LH_2 target. The parameters c_R, h_R, x_R, w_R and c_L were the same for all the peaks in the spectrum, and for all the angles with the same beam tune. They were determined at angles where the peaks were well separated, and were kept fixed at angles where the peaks overlapped. The parameters b_R and b_L were treated in several ways: they were fixed or allowed to vary both with the angle and for the peaks in the spectrum. The differences between the results obtained in the different methods of separating the peaks were used to estimate the uncertainties introduced by the peak separation procedure.

Appendix D. Acceptance

The slow variation of the detection efficiency results from the spectrometer optics, in particular from the change of the detection solid angle with momentum. The typical MRS acceptance is linear in the middle of the focal plane, and quickly falls at the ends. In the present experiment this slow variation was essentially eliminated by the very small entrance window of the spectrometer defined by software windows on the $X0$ and $Y0$ positions in the FEC chambers. Nearly all the protons from this entrance window were detected above the focal plane of the spectrometer. The dependence of the detection efficiency on $\rho = p/B$ was checked using protons elastically scattered from the aluminum target at 11°. The magnetic field of the spectrometer was changed to shift the elastic scattering peak through the focal plane. The number of protons registered in the MRS, corrected for the dead time measured with a pulser, divided by the number of counts from the beam integrator provided a measure of the spectrometer acceptance. The acceptance was found to be independent of the magnetic induction B, and hence independent of XF to within 1%. The beam current monitor, detected in coincidence two protons from the proton-proton scattering in the CH_2 target. Four pairs of proton detectors were used (left, right, up and down) which reduced sensitivity of the counting rate to the beam position. The results of the acceptance curve measurements are shown in fig. 14.

The experimental results were based on the comparison of the proton yields at different momenta, so the local variations of the detection efficiency across the focal plane were very important. Such variations could be produced by lower efficiency of particular wires of the VDC chambers, especially in the X1 chamber situated close to the focal plane. The 6 mm inter-wire spacing in the VDC chambers at $E_r = 198.5$ MeV corresponds to a 380 keV energy step which is important for analysis of the shape of the d^* resonance.

Information from the VDC chambers was analysed in a way which largely reduced possible irregularities of the response functions due to inefficient wires. Particles passing the VDCs at an angle of $\sim 45°$ typically produce signals in 4 to 5 wires. The timing of pulses from the wires is used for the precise determination of the hit position. The software used for analysis of the data identified cases with one wire in the cluster missing and calculated hit positions using timing information from the active wires. The program also provided spectra of the inefficiency of each wire in the VDCs. On the other hand it rejected cases for which the time pattern from the wires indicated production of δ rays, which could result in an incorrect determination of the hit position. With this software the VDCs inefficiency was about 2% per chamber practically independent of the position. The total inefficiency for detection in the focal plane was about 4%, because information from the two X chambers but only one of the U chambers was required.

The homogeneity of the MRS response function was checked by measuring a smooth continuous spectrum from high excitations obtained by bombarding the LD_2 target at 456.6 MeV. The spectrum was measured for ten values of the MRS field B to average over possible variations of the (p, p') cross sections. The summed spectrum is shown in fig. 15 with a fitted quadratic function of XF. Only few points measured with the statistical error of 0.35% deviate from the curve by more than 0.5%. The origin of the small structure around position 520 mm is difficult to explain, as the program did not indicate any unusually inefficient wires in the VDCs. This structure did not disturb the precise measurements of the shape of the d^* resonance significantly, because the $\sigma_{p,p'}$ spectra were measured for six values of the magnetic field and less than a third of the data overlaps the affected region. Moreover, because of the kinematic shift of the spectra with Θ, the effect of the structure in the response function on their shape partly averages out even for the runs for which overlapping takes place.

Appendix E. NN scattering amplitudes

The nucleon-nucleon scattering amplitude can be expressed in terms of the scattering matrix in the total spin representation:

$$t^{m_1 m_1'}_{m_2 m_2'}(\Theta) = \sum_S < s_1 m_1 s_2 m_2 | SM >< s_1 m_1' s_2 m_2' | SM' >< SM \parallel t \parallel SM' > \quad \text{(E.1)}$$

where S is the total spin of two nucleons involved in the scattering.

On the other hand this scattering amplitude can be developed as a sum of the irreducible tensors $B^{m_1 m_1'}_{s m_s}(\Theta)$:

$$t^{m_1 m_1'}_{m_2 m_2'}(\Theta) = \sum_s < s_2 m_2 s m_s | s_2 m_2' > \frac{\hat{S}^2}{\hat{s}_2^2} B^{m_1 m_1'}_{s m_s}(\Theta) \quad \text{(E.2)}$$

where the s is the spin transferred to the struck nucleon.

The irreducible tensors can be obtained from the scattering matrix elements using the formula:

$$B^{m_1 m_1'}_{s m_s}(\Theta) = \sum_{m_2'' m_2'''} < s_2 m_2'' s m_s | s_2 m_2''' >< s_1 m_1 s_2 m_2'' | SM >< s_1 m_1' s_2 m_2''' | SM' > \\ < SM \parallel t \parallel SM' > \quad \text{(E.3)}$$

A standard and simplest way to express the nucleon-nucleon scattering amplitude is to use the Wolfenstein[31]) amplitudes:

$$t(\Theta) = A(\Theta) + M(\Theta)\sigma_{1n}\sigma_{2n} + C(\Theta)(\sigma_{1n} + \sigma_{2n}) + G(\Theta)(\sigma_{1q}\sigma_{2q} + \sigma_{1p}\sigma_{2p}) + H(\Theta)(\sigma_{1p}\sigma_{2p} - \sigma_{1q}\sigma_{2q}) \qquad (E.4)$$

where the directions of $\vec{n}, \vec{q}, \vec{p}$ are defined by the vectors $\vec{p_i} \times \vec{p_f}, \vec{p_f} - \vec{p_i}$ and $\vec{p_f} + \vec{p_i}$, and subscripts 1 and 2 denote two nucleons involved in the scattering. From the nucleon-nucleon amplitudes are constructed the irreducible tensors which depend on the spin magnetic numbers of a scattered nucleon m_1 and m_1', and the spin transfer and its magnetic number. Relations between elements of the scattering matrix and the Wolfenstein amplitudes are given in ref.[31]).

The explicit formulae for the irreducible tensors $B_{sm_s}^{m_1 m_1'}(\Theta)$ as functions of the Wolfenstein[31]) amplitudes of the nucleon-nucleon scattering are the following:

$$\begin{aligned}
B_{00}^{\frac{1}{2}\frac{1}{2}}(\Theta) &= B_{00}^{-\frac{1}{2}-\frac{1}{2}}(\Theta) = 2A(\Theta) \\
B_{10}^{\frac{1}{2}\frac{1}{2}}(\Theta) &= -B_{10}^{-\frac{1}{2}-\frac{1}{2}}(\Theta) = -\frac{2}{\sqrt{3}}(G(\Theta) + H(\Theta)\cos(\Theta)) \\
B_{11}^{\frac{1}{2}\frac{1}{2}}(\Theta) &= B_{1-1}^{-\frac{1}{2}-\frac{1}{2}}(\Theta) = -\sqrt{\frac{2}{3}}(H(\Theta)\sin(\Theta) + iC(\Theta)) \\
B_{1-1}^{\frac{1}{2}\frac{1}{2}}(\Theta) &= B_{11}^{-\frac{1}{2}-\frac{1}{2}}(\Theta) = \sqrt{\frac{2}{3}}(H(\Theta)\sin(\Theta) - iC(\Theta)) \\
B_{00}^{\frac{1}{2}-\frac{1}{2}}(\Theta) &= B_{00}^{-\frac{1}{2}\frac{1}{2}}(\Theta) = -2iC(\Theta) \\
B_{10}^{\frac{1}{2}-\frac{1}{2}}(\Theta) &= B_{10}^{-\frac{1}{2}\frac{1}{2}}(\Theta) = \frac{2}{\sqrt{3}}H(\Theta)\sin(\Theta) \\
B_{1-1}^{\frac{1}{2}-\frac{1}{2}}(\Theta) &= B_{11}^{-\frac{1}{2}\frac{1}{2}}(\Theta) = \sqrt{\frac{2}{3}}(G(\Theta) - M(\Theta) - H(\Theta)\cos(\Theta)) \\
B_{11}^{\frac{1}{2}-\frac{1}{2}}(\Theta) &= -B_{1-1}^{-\frac{1}{2}\frac{1}{2}}(\Theta) = \sqrt{\frac{2}{3}}(-M(\Theta) - G(\Theta) + H(\Theta)\cos(\Theta))
\end{aligned} \qquad (E.5)$$

The amplitudes used in this equation are sums or differences of the proton-proton and proton-neutron scattering amplitudes: $A(\Theta) = A_{p-p}(\Theta) \pm A_{n-p}(\Theta)$ and so on. The relative sign with which these amplitudes are added is given by the factor $(-)^{l-s_D-s_D'}$ derived from the symmetry properties of the spherical harmonics and the C-G coefficients. In elastic scattering, for which l is an even number and $s_D = s_D' = 1$ amplitudes are added with the same sign, and in inelastic scattering leading to the d^* resonance ($l = 0, s_D'$=0) the signs are opposite.

6. Acknowledgements

The authors gratefully acknowledge the assistance of many individuals in the successful completion of this experiment. The cryogenic target was designed, constructed and operated by C. Marshall under the direction of D. Healey. C.A. Miller and M. Vetterli assisted in preliminary experiments and provided valuable expertise in the operation of the spectrometer. A. Warburton helped develop the program used to optimize the efficiencies of the wire chambers. S.Ram participated in the preliminary phase of this experiment. The TRIUMF staff provided excellent technical support throughout.

We also wish to thank A. Gal, R. Machleidt and Sir. D. Wilkinson for their advice and encouragement in the interpretation of the data. B. Loiseau kindly provided the software necessary to utilize the Paris potential in the analysis. We have been stimulated by discussions with W. Glöckle, H. Witala and B. Vlahovic regarding the possible interpretation of these data using a rigorous three-body formalism.

This work was supported by grants from the Natural Sciences and Engineering Research Council of Canada and by the European Community Contract C11-CT-91-0894.

7. References

1) J.N. Bahcall *et al.*, Rev. Mod. Phys. 54 (1982) 767.
2) G.F. Chew and G.C. Wick Phys. Rev. 83 (1952) 636.
3) A.K. Kerman, H. McManus and R.M. Thaler, Ann. Phys. 8 (1959) 551.
4) A.H. Cromer, Phys. Rev. 129 (1963) 1680.
5) D.G. Stairs, R. Wilson and P.F. Cooper Jr., Phys. Rev. 129 (1963) 1672.
6) K. Kuroda *et al.*, Physics Letters 16 (1965) 133.
7) G.A. Miller, B.M.K. Nefkens and I. Šlaus Phys. Rep. 194 (1990) 1.
8) I. Šlaus, Y. Akaishi and H. Tanaka, Phys. Rep. 173 (1989) 257.
9) B. Gabioud *et al.*, Nucl. Phys. A420 (1984) 496.
10) O. Schori *et al.*, Phys. Rev. C35 (1987) 2252.
11) H. Sakai *et al.*, Phys. Rev. C35 (1987) 344.
12) H. Witala, W. Glöckle and Th. Cornelius, Nucl. Phys. A496 (1989) 446.
13) W. Glöckle *et al.*, in preparation.
14) O. Dumbrajs *et al.*, Nucl. Phys. B216 (1983) 277.
15) S.A. Coon and M.D. Scadron, Phys. Rev. C26 (1982) 2402.
16) R. Machleidt, Adv. in Nucl. Phys. 19 (1989) 189.
17) R.A. Arndt, Scattering analysis interactive dial-in (SAID) program, and R.A. Arndt *et al.*, Phys. Rev. D45 (1992) 3995.
18) J. Carbonell, M.B. Barbaro and C. Wilkin, Nucl. Phys. A529 (1991) 653.
19) M. Lacombe *et al.*, Phys. Rev. C21 (1980) 861.
20) R. Machleidt, K. Holinde and Ch. Elster Phys. Rep. 149 (1987) 1.
21) E.T. Boschitz *et al.*, Phys. Rev. C6 (1972) 457.
22) J. Fain *et al.*, Nucl. Phys. A262 (1976) 413.
23) F. Irom *et al.*,, Phys. Rev. C28 (1983) 2380.
24) O.G. Grebenjuk *et al.*, Nucl. Phys. A500 (1989) 637.

25) G. Alberi, M. Bleszynski, T. Jaroszewicz, Ann. of Phys. 142 (1982) 299.
26) G. Igo *et al.*, Phys. Rev. C38 (1988) 2777.
27) D.L. Adams and M.Bleszynski, Phys. Lett. 150B (1985) 405.
28) C. Ellegaard *et al.*, Phys. Rev. Lett. 59 (1987) 974.
29) D.V. Bugg and C. Wilkin, Nucl. Phys. A467 (1987) 575.
30) S. Kox *et al.*,, Phys. Lett. B 266 (1991) 264.
31) N. Hoshizaki, Suppl. Prog. Theo. Phys. 42 (1968) 107.

Table 1. Ratios of differential cross sections for elastic scattering

198.5 MeV		297.6 MeV		456.6 MeV	
Θ	σ_{pd}/σ_{pp}	Θ	σ_{pd}/σ_{pp}	Θ	σ_{pd}/σ_{pp}
3.13	0.837 ± 0.060	2.96	1.286 ± 0.050	2.88	2.042 ± 0.024
3.40	0.946 ± 0.040	3.23	1.389 ± 0.040	3.15	2.142 ± 0.024
3.66	1.101 ± 0.030	3.50	1.499 ± 0.035	3.42	2.176 ± 0.025
3.93	1.285 ± 0.015	3.76	1.641 ± 0.030	3.68	2.215 ± 0.026
4.18	1.442 ± 0.014	4.01	1.731 ± 0.016	3.92	2.218 ± 0.020
4.44	1.535 ± 0.016	4.28	1.808 ± 0.016	4.19	2.226 ± 0.021
4.71	1.695 ± 0.018	4.55	1.836 ± 0.016	4.45	2.227 ± 0.021
4.97	1.743 ± 0.019	4.82	1.882 ± 0.016	4.71	2.158 ± 0.021
5.13	1.867 ± 0.013	5.00	1.908 ± 0.013	4.90	2.175 ± 0.018
5.24	1.849 ± 0.020	5.08	1.891 ± 0.016	4.99	2.128 ± 0.021
5.42	1.933 ± 0.012	5.30	1.950 ± 0.011	5.19	2.132 ± 0.016
5.69	1.989 ± 0.012	5.57	1.933 ± 0.011	5.46	2.093 ± 0.014
5.96	2.010 ± 0.012	5.83	1.924 ± 0.011	5.72	2.067 ± 0.014
6.23	2.007 ± 0.012	6.10	1.914 ± 0.011	6.00	1.977 ± 0.014
6.43	2.065 ± 0.012	6.27	1.894 ± 0.012	6.17	1.945 ± 0.015
6.70	2.026 ± 0.012	6.54	1.863 ± 0.013	6.44	1.880 ± 0.013
6.96	2.003 ± 0.012	6.80	1.831 ± 0.014	6.71	1.821 ± 0.013
7.23	2.011 ± 0.012	7.07	1.796 ± 0.017	6.98	1.788 ± 0.013
7.62	1.947 ± 0.017	7.49	1.757 ± 0.013	7.17	1.780 ± 0.022
7.92	1.967 ± 0.015	7.76	1.693 ± 0.013	7.40	1.708 ± 0.012
8.18	1.920 ± 0.015	8.03	1.651 ± 0.013	7.66	1.661 ± 0.013
8.46	1.864 ± 0.015	8.30	1.621 ± 0.013	7.94	1.586 ± 0.012
8.69	1.818 ± 0.016	8.53	1.601 ± 0.015	8.20	1.557 ± 0.012
8.93	1.812 ± 0.013	8.73	1.522 ± 0.013	8.43	1.485 ± 0.012
9.19	1.788 ± 0.013	8.80	1.545 ± 0.014	8.66	1.455 ± 0.010
9.46	1.736 ± 0.012	9.03	1.498 ± 0.010	8.93	1.420 ± 0.010
9.75	1.680 ± 0.015	9.26	1.473 ± 0.010	9.19	1.374 ± 0.010
9.96	1.679 ± 0.020	9.57	1.420 ± 0.010	9.46	1.333 ± 0.009
10.18	1.650 ± 0.011	9.80	1.383 ± 0.012	9.67	1.255 ± 0.013
10.44	1.655 ± 0.010	10.00	1.387 ± 0.008	9.91	1.256 ± 0.010
10.71	1.575 ± 0.010	10.28	1.310 ± 0.008	10.18	1.190 ± 0.008
10.98	1.529 ± 0.010	10.54	1.296 ± 0.008	10.45	1.149 ± 0.008
11.20	1.500 ± 0.011	10.82	1.237 ± 0.008	10.72	1.096 ± 0.010
11.54	1.449 ± 0.009	11.04	1.229 ± 0.009	10.95	1.057 ± 0.010
11.81	1.395 ± 0.009	11.25	1.192 ± 0.007	11.28	1.014 ± 0.008
12.00	1.358 ± 0.011	11.52	1.168 ± 0.006	11.55	0.974 ± 0.008
12.21	1.351 ± 0.010	11.79	1.119 ± 0.007	11.82	0.944 ± 0.007

Table 1 con't

198.5 MeV		297.6 MeV		456.6 MeV	
Θ	σ_{pd}/σ_{pp}	Θ	σ_{pd}/σ_{pp}	Θ	σ_{pd}/σ_{pp}
12.42	1.339 ± 0.014	12.05	1.090 ± 0.008	12.09	0.907 ± 0.007
12.69	1.275 ± 0.013	12.28	1.048 ± 0.008	12.43	0.879 ± 0.010
12.96	1.262 ± 0.013	12.54	1.025 ± 0.008	12.69	0.823 ± 0.009
13.22	1.211 ± 0.013	12.81	1.004 ± 0.009	12.96	0.779 ± 0.009
13.49	1.136 ± 0.012	13.08	0.954 ± 0.009	13.22	0.752 ± 0.009
13.76	1.153 ± 0.012	13.34	0.920 ± 0.009	13.49	0.711 ± 0.009

Table 2. Derived ratios of the inelastic scattering populating the $^1S_0$ np states to the elastic pp scattering.

198.5 MeV		297.6 MeV		456.6 MeV	
Θ	$\sigma_{pd^*}/\sigma_{pp}$	Θ	$\sigma_{pd^*}/\sigma_{pp}$	Θ	$\sigma_{pd^*}/\sigma_{pp}$
3.02	0.258 ± 0.029	2.87	0.341 ± 0.020	3.06	0.345 ± 0.006
3.28	0.340 ± 0.014	3.14	0.411 ± 0.012	3.33	0.348 ± 0.006
3.55	0.455 ± 0.011	3.41	0.460 ± 0.012	3.59	0.357 ± 0.006
3.82	0.552 ± 0.009	3.67	0.505 ± 0.012	3.86	0.341 ± 0.007
4.08	0.613 ± 0.008	3.94	0.533 ± 0.011	4.13	0.341 ± 0.007
4.35	0.646 ± 0.008	4.21	0.532 ± 0.011	4.39	0.323 ± 0.007
4.62	0.671 ± 0.009	4.47	0.535 ± 0.011	4.66	0.302 ± 0.007
4.88	0.669 ± 0.009	4.74	0.518 ± 0.011	4.93	0.291 ± 0.006
4.90	0.670 ± 0.009	4.63	0.525 ± 0.011	4.84	0.297 ± 0.007
5.16	0.681 ± 0.008	4.89	0.514 ± 0.011	5.10	0.291 ± 0.007
5.43	0.679 ± 0.008	5.16	0.502 ± 0.010	5.37	0.278 ± 0.007
5.70	0.667 ± 0.008	5.43	0.492 ± 0.010	5.64	0.267 ± 0.007
5.96	0.646 ± 0.007	5.69	0.471 ± 0.010	5.90	0.254 ± 0.007
6.23	0.623 ± 0.007	5.96	0.457 ± 0.010	6.17	0.249 ± 0.007
6.50	0.606 ± 0.006	6.23	0.442 ± 0.010	6.43	0.223 ± 0.007
6.77	0.579 ± 0.006	6.50	0.427 ± 0.009	6.70	0.222 ± 0.007
7.03	0.555 ± 0.006	6.76	0.410 ± 0.009	6.97	0.209 ± 0.007
7.22	0.546 ± 0.007	7.08	0.399 ± 0.010	7.29	0.205 ± 0.007
7.49	0.523 ± 0.007	7.35	0.380 ± 0.010	7.56	0.197 ± 0.007
7.76	0.499 ± 0.007	7.62	0.365 ± 0.010	7.83	0.188 ± 0.007
8.02	0.488 ± 0.007	7.88	0.351 ± 0.010	8.09	0.183 ± 0.007
8.29	0.469 ± 0.008	8.15	0.340 ± 0.010	8.36	0.176 ± 0.007
8.56	0.449 ± 0.008	8.41	0.327 ± 0.010	8.63	0.162 ± 0.008
8.82	0.436 ± 0.008	8.68	0.307 ± 0.010	8.90	0.165 ± 0.008
9.09	0.422 ± 0.009	8.95	0.301 ± 0.010	9.16	0.157 ± 0.008
9.36	0.408 ± 0.009	9.22	0.289 ± 0.010	9.43	0.154 ± 0.008
9.90	0.379 ± 0.010	9.65	0.276 ± 0.010	9.83	0.146 ± 0.008
10.17	0.365 ± 0.009	9.92	0.272 ± 0.010	10.09	0.140 ± 0.008
10.43	0.373 ± 0.009	10.18	0.261 ± 0.010	10.36	0.133 ± 0.008
10.70	0.347 ± 0.009	10.45	0.252 ± 0.010	10.63	0.131 ± 0.008
10.97	0.342 ± 0.009	10.72	0.244 ± 0.010	10.89	0.126 ± 0.008
11.23	0.331 ± 0.010	10.99	0.241 ± 0.010	11.16	0.123 ± 0.008
11.50	0.322 ± 0.010	11.25	0.231 ± 0.010	11.43	0.117 ± 0.008
11.77	0.308 ± 0.010	11.52	0.238 ± 0.010	11.70	0.113 ± 0.008
12.04	0.295 ± 0.010	11.79	0.218 ± 0.010	11.96	0.112 ± 0.008

Table 3. χ^2 analysis of IA fits to the data of fig. 9.

Θ	4.08	6.50	9.09
a_{np} (fm)	-23.75^*	-23.75^*	-23.75^*
$\Delta\varepsilon$ (keV)	0^*	0^*	0^*
D. of F.	85	85	85
χ^2_1	92.4	77.44	102.68
a_{np} (fm)	-24.59 ± 0.24	-24.64 ± 0.24	-25.13 ± 0.44
$\Delta\varepsilon$ (keV)	0^*	0^*	0^*
D. of F.	84	84	84
χ^2_2	79.88	62.12	91.98
a_{np} (fm)	-24.27 ± 0.34	-24.85 ± 0.36	-25.90 ± 0.85
$\Delta\varepsilon$ (keV)	-1.3 ± 1.0	0.9 ± 1.1	3.2 ± 3.0
D. of F.	83	83	83
χ^2_3	79.01	61.50	89.64

*parameter is fixed at given value

Figure captions

1. Schematic view of the experimental configuration.

2. Portions of typical spectra used to determine σ_{pd}/σ_{pp} with the mixed LD_2/LH_2 target.

3. The measured ratios σ_{pd}/σ_{pp} (data and non-systematic errors in upper panels). The predictions of the IA are shown based on the NN amplitudes given by SM90 (solid lines) and the Bonn potential (dashed lines). The lower panels show predictions of σ_{pd} and σ_{pp} separately.

4. Typical proton spectrum recorded with the LD_2 target.

5. Typical results for $\sigma_{pd'}$ in the region of the np threshold. The solid curves fitted to the data with one normalization parameter are the predictions of the IA (see subsect. 5.2). The lower curves are predictions for all final states excluding the d^* ($^1S_0$).

6. Data are ratios of the measured ratios σ_{pd}/σ_{pp} to the ratios predicted in the IA using the NN amplitudes of SM90. The curves correspond to predictions with other NN amplitudes: FA91 global solution (solid), Bonn potential (long dashes), Paris potential (dot-dash), Arndt V350 (short dashes) and local Arndt (dots).

7. Data are normalization factors required to fit observed $\sigma_{pd'}(\varepsilon)/\sigma_{pp}$ to IA predictions with SM90. The predictions based on other NN amplitudes are represented as in fig. 6.

8. Upper panels: estimated ratios $\sigma_{pd^*}/\sigma_{pp}$ compared with IA predictions with NN interactions given by SM90 (solid lines) and Bonn potential (dashed lines). Lower panels: separate predictions of σ_{pp} and σ_{pd^*}.

9. Upper panels: examples of the $d(p,p')$ data used in the analysis of a_{np}. The solid curves are IA fits with variable normalization but with a_{np}=-23.748 fm. As in fig. 5 the lower curves in these panels are for all final states except d^*. Lower panels: individual points are the differences between the data and solid curve above. The results of fits to the data achieved with a_{np} as a variable parameter (see text) are indicated by the dashed ($\Delta\varepsilon = 0$) and dot-dashed ($\Delta\varepsilon$ variable) curves. The significance of these refinements can be best assessed with reference to table 3.

10. Values of the scattering length fitted using the IA to $\sigma_{pd'}(\varepsilon)$ for three values of the upper limit on ε. Solids points with $\Delta\varepsilon = 0$; open circles with $\Delta\varepsilon$ variable. Solid lines represent the known value of a_{np} and the vertical dashed lines enclose the fitted values rejected on the basis of a weak contamination from the $H(p,p_0)$ reaction (see text).

11. Average values of a_{np} derived from the data of fig. 10 plotted as a function of the maximum value of ε included in fit. Solids points with $\Delta\varepsilon = 0$; open circles with $\Delta\varepsilon$ as a free parameter at each value of Θ. The double line represents the known value a_{np} = -23.748 fm. The cross-hatched region shows the a_{np} = 24.7 ± 0.4 fm value obtained from this analysis.

12. Calibration of the MRS focal plane at E_i = 198.5 MeV. $\Delta\omega$ is the difference between the measured and fitted positions of the peaks. Points corresponding to population of different final states in ^{12}C are: solid diamond (0.0 keV), solid triangle (4438.9 keV), solid circle (7654.2 keV) and open circle (15110 keV).

13. Measured and fitted lineshapes for the elastic scattering on the aluminum windows and deuterium in the LD_2 target. The dotted curve shows the result of the fit with the last factor in eq. (C.1) set to 1.

14. MRS acceptance measured by elastic scattering on aluminum at different values of the magnetic field in the dipole.

15. Local variations of the MRS acceptance measured with the (p,p') continuum at $\omega \sim 260$ MeV. The data at each point on the focal plane (XF) represent the sum of 10 measurements taken at different values of the magnetic field in the dipole.

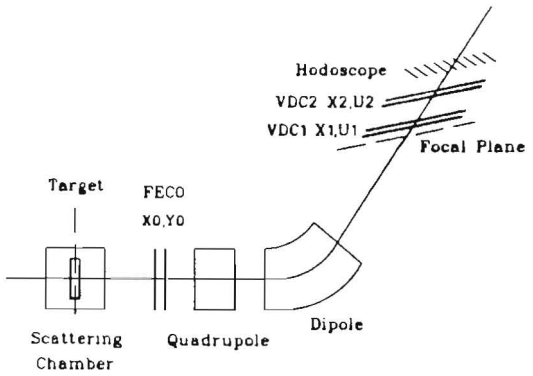

Fig.1

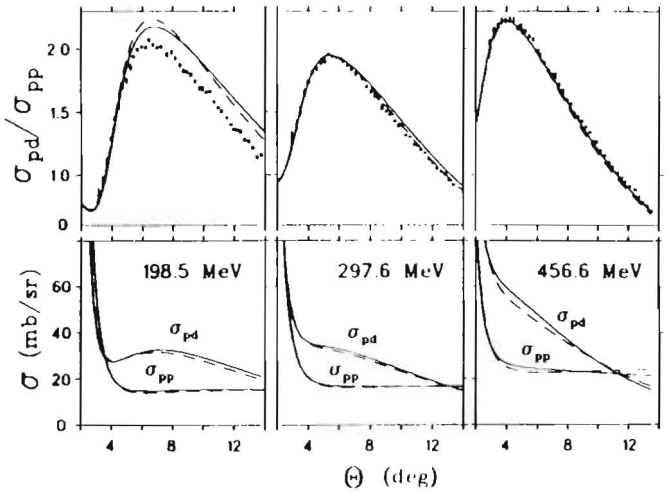

Fig.3

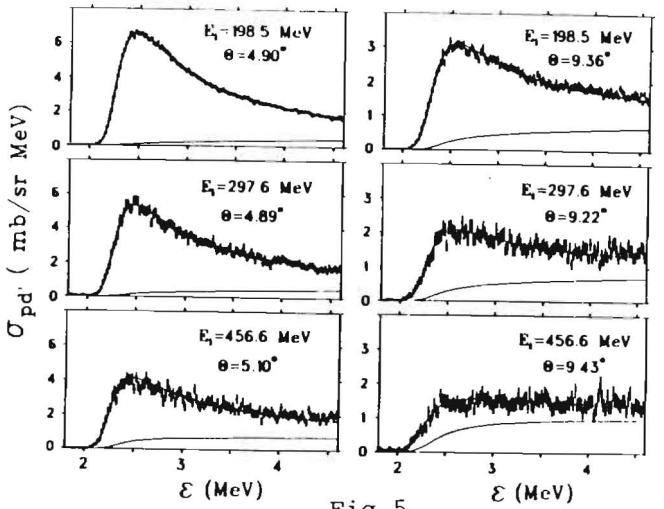

Fig.5

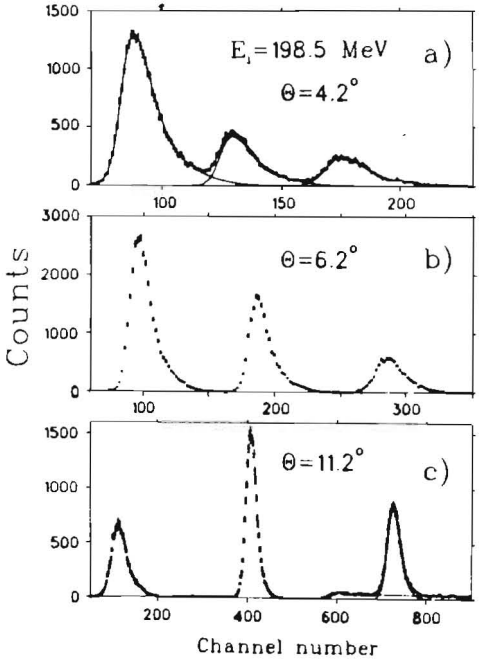

Fig.2

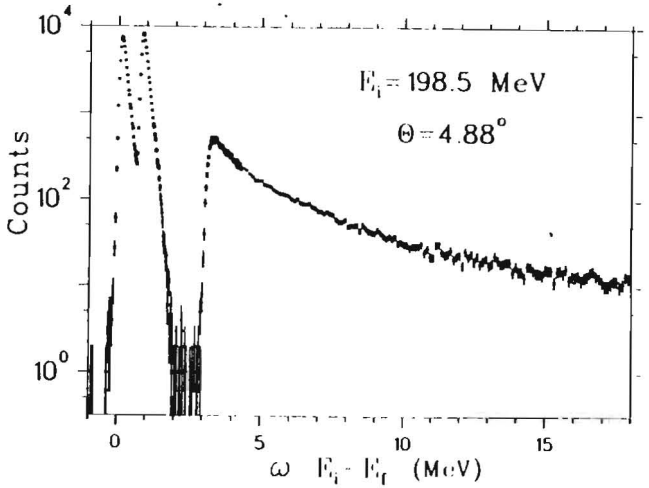

Fig.4

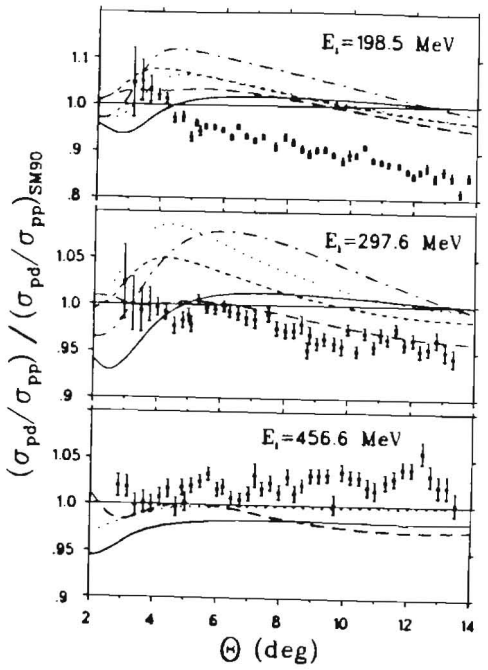

Fig.6

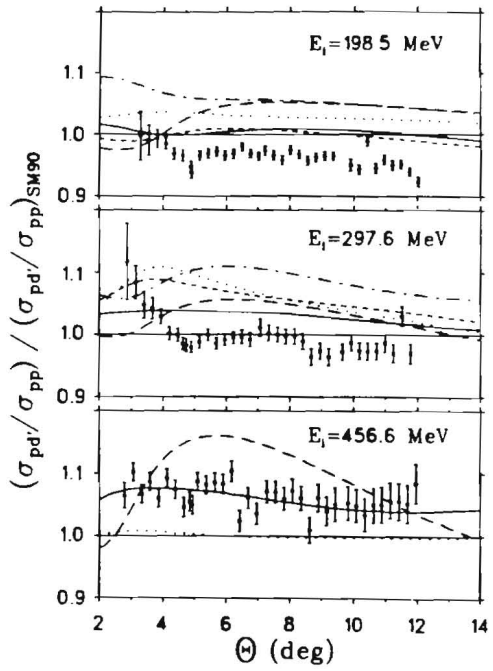

Fig.7

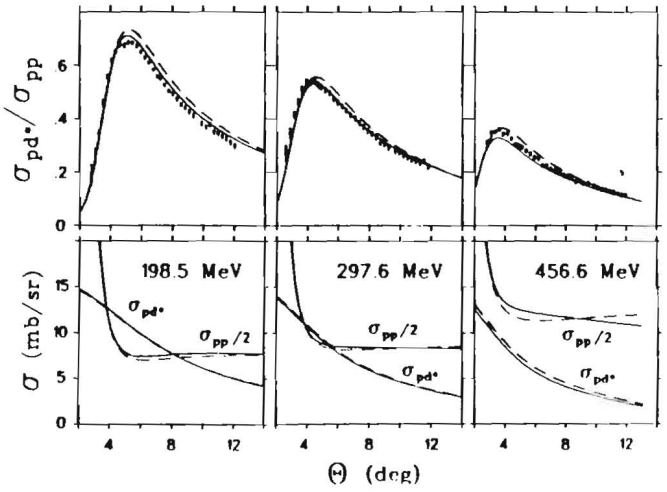

Fig.8

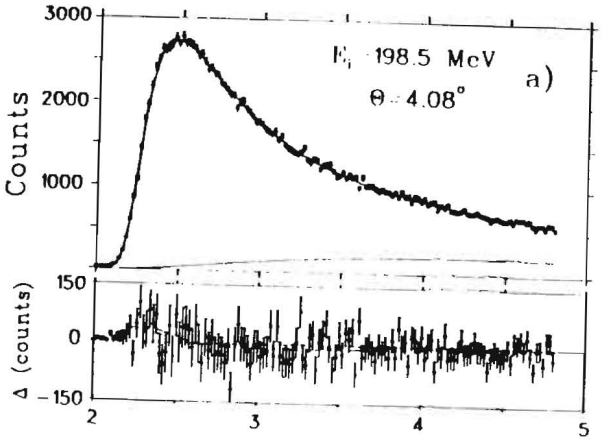

Fig.9a

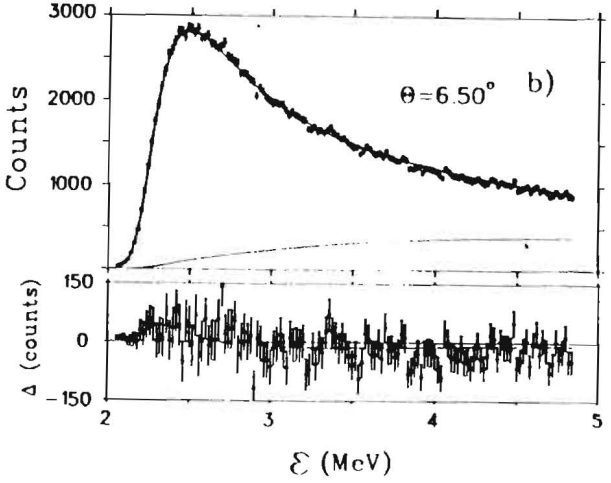

Fig.9b

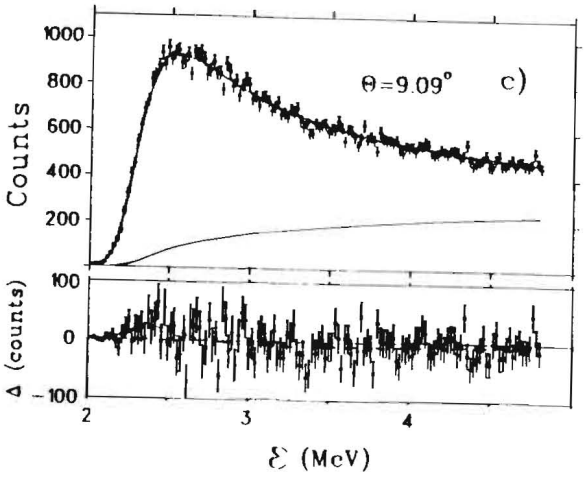

Fig.9c

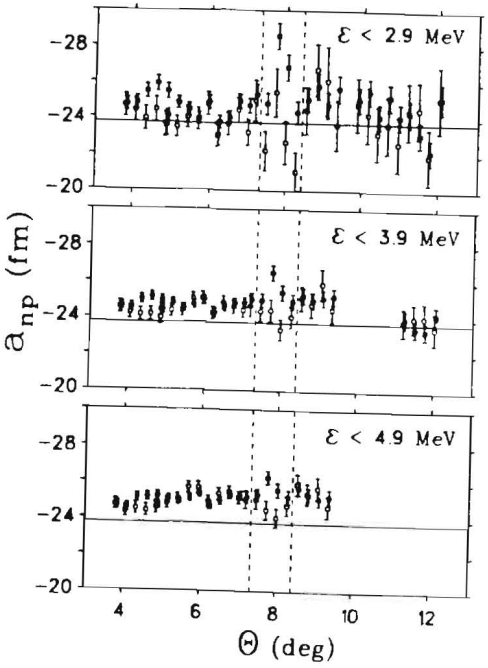

Fig.10

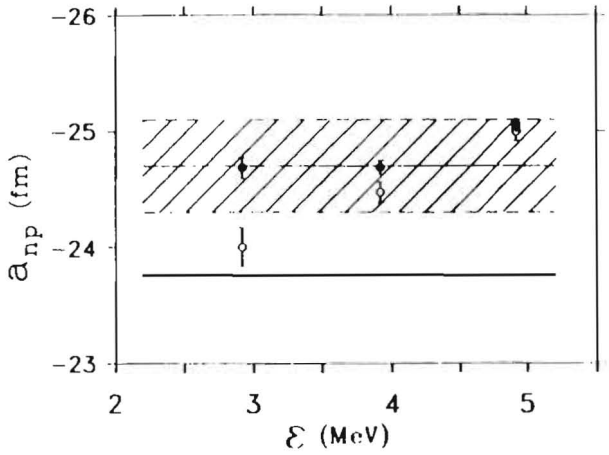

Fig.11

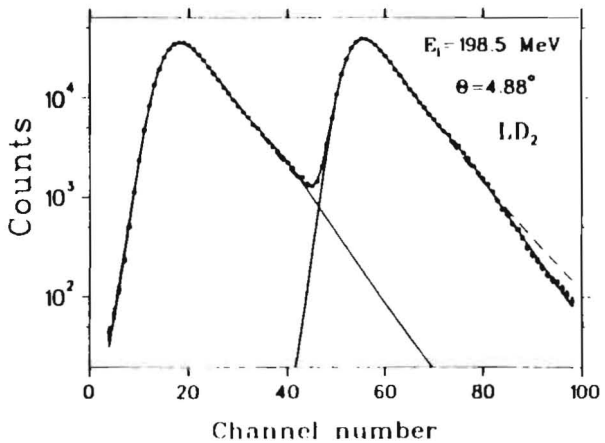

Fig.13

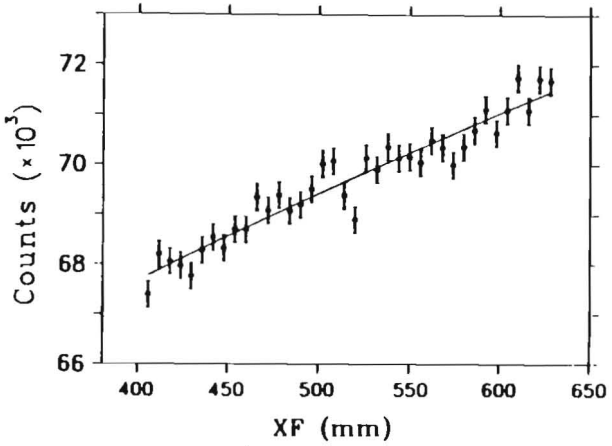

Fig.15

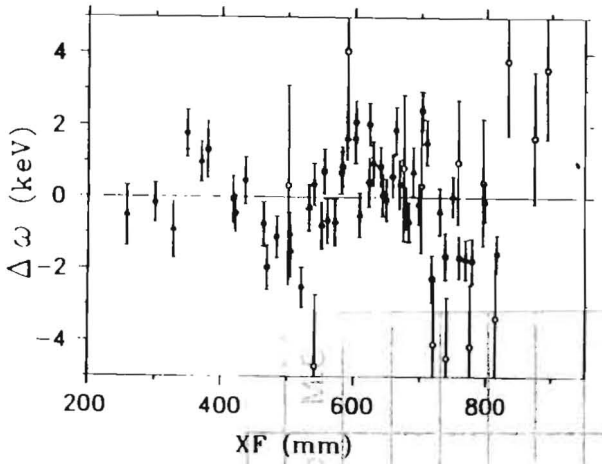

Fig.12

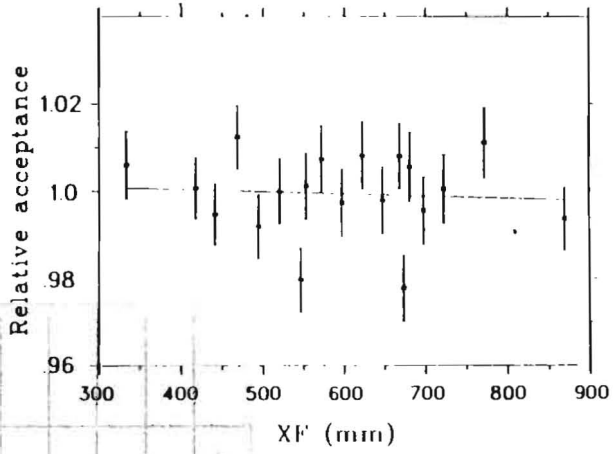

Fig.14